HIGH PERFORMANCE DUAL SHAPED REFLECTOR ANTENNAS FOR EARTH STATIONS

KAIJUN GU

HIGH PERFORMANCE DUAL SHAPED REFLECTOR ANTENNAS FOR EARTH STATIONS

By

© Kaijun Gu

A thesis submitted to the School of Graduate Studies
in partial fulfillment of the requirements for the degree of
Master of Engineering

Faculty of Engineering and Applied Science
Memorial University of Newfoundland
March, 1995

St. John's Newfoundland Canada

National Library
of Canada

Acquisitions and
Bibliographic Services Branch

395 Wellington Street
Ottawa, Ontario
K1A 0N4

Bibliothèque nationale
du Canada

Direction des acquisitions et
des services bibliographiques

395, rue Wellington
Ottawa (Ontario)
K1A 0N4

Your file Votre référence

Our file Notre référence

ISBN 0-612-06123-X

Canadä

Abstract

In satellite communications, the earth station antenna plays a major role in the vital link between the satellite and the earth station electronic equipment. In this thesis, dual shaped reflector antennas for earth stations which can provide a pencil beam toward a geostationary satellite are introduced. The design and analysis of both Cassegrain and Gregorian antennas are presented as follows.

(i) The high performance antenna feeds are studied in detail. Various specific characteristics required in Cassegrain and Gregorian antennas are discussed and it is shown that the corrugated conical horn is the best choice.

(ii) The computer aided synthesis of subreflector and main reflector are developed by using the geometric optics (GO) approach. Given the feed radiation pattern and the desired main reflector aperture power illumination, the sub and main reflectors can be shaped to obtain optimal reflector profiles.

(iii) After having the sub and main reflector profiles, the physical optics (PO) are used to calculate the scattered pattern of the subreflector, the radiation patterns as well as the whole antenna specifications.

(iv) A number of power distributions on the main reflector aperture are investigated to maximize the boresight gain and at the same time, minimize the sidelobe levels. A pattern control method is also developed.

(v) Performance comparison between Cassegrain antenna and Gregorian antenna is also made.

The major contribution of this thesis is the complete computer aided design tool for a very high performance antenna.

Acknowledgements

I would like to express my deepest gratitude to my supervisor Dr. Son LeNgoc, for all his guidance, advice and assistance during the course of my graduate studies and the writing up of the thesis.

The financial support from the Faculty of Engineering and Applied Science and NSERC is gratefully acknowledged.

The last but not least, I would like to give my special thanks to my wonderful wife, Yi Zhang, for her patience and help during my M.Eng program.

Contents

List of Figures

List of Principal Symbols and Abbreviations

$\vec{A}$	vector potential in conical horn
$\vec{E}$	electric field
E_c	co-polarized electric field component
E_X	cross-polarized electric field component
$\vec{F}$	vector potential in conical horn
$F(\theta)$	feed radiation pattern
G	antenna gain
$h_n^2(x)$	spherical Hankel function of 2nd kind and order n
$\vec{H}$	magnetic field
$I(x)$	aperture power illumination
$\vec{J}$	surface current
$J_m(x)$	Bessel function of 1st kind and order m
k	free space wave number
P_A	main reflector aperture power density
$P_n^m(\cos\theta)$	associated Legendre function of 1st kind and order n
$Q_n^m(\cos\theta)$	associated Legendre function of 2nd kind and order n
$Y_m(x)$	Bessel function of 2st kind and order m
δZ_f	distance between origins of feed and subreflector coordinates
δZ_m	distance between origins of main and subreflector coordinates
β	propagation constant in the lossless medium
ϵ_0	free space permittivity
η	antenna efficiency

Γ	normalized hybrid factor
λ	wavelength
μ_0	free space permeability
ω	angular frequency
GO	geometrical optics
PO	physical optics

Chapter 1

Introduction

1.1 Statement of the Problem

Pencil-beam antennas are most widely used in point-to-point and point-to-multipoint microwave communication systems. In terrestrial microwave relay systems, the beam of one antenna is fixed and directed to another antenna for each hop along the path at the time of installation, while in satellite communication systems, the beam of the earth station antenna is pointed directly to the satellite. With high gain and creating no noise, the antenna plays an important role in the vital link between two repeaters or two earth stations. One can conclude that there would be no satellite communications if there were no antenna.

It has become a common practice to focus microwave energy into a desired beam by the use of metallic reflecting surface (or surfaces) excited by radiation from a small, relatively non-directional microwave source. These kinds of antennas are called reflector antennas. In the family of reflector antennas, one distinguished member is the dual reflector antenna, especially the axisymmetrical dual- reflector antenna. The axisymmetrical dual-reflector antenna has numerous mechanical and electrical advantages over the conventional focal-point fed large paraboloidal antennas. The Cassegrain antenna is one kind of dual-reflector antennas derived from the telescope design of William Cassegrain. It has a hyperboloidal subreflector and a paraboloidal main reflector. This kind of antenna had a long history and still is the most commonly used earth station antenna today.

Because of the importance and wide applications of the Cassegrain antenna, the antenna design is always an interesting topic in satellite communications. Owing to the high cost, these earth station antennas are normally designed and optimized such that the very stringent requirement of CCITT (International Telegraph and Telephone Consultative Committee) is met and yet the high gain and the low sidelobe levels are still achieved. In addition, the close-in sidelobe requirement is even more critical when the geostationary orbit is getting more and more congested every day.

The dual-reflector antenna consists of the feed, subreflector and main reflector. To achieve the desired specifications, such as the boresight gain, sidelobe levels, antenna efficiency, cross-polarization levels, etc., the feed must be designed to provide a suitable radiation pattern as well, the two reflectors should be shaped in such a way that the desired aperture power illumination is obtained. For these reasons, the computer-aided-design (CAD) and the computer-aided-analysis (CAA) of the dual reflector antennas have been the popular topic in recent years. The CAD and CAA tools are normally needed for the satellite communication engineering.

One of the variations of the Cassegrain antenna is the Gregorian antenna in which the hyperboloidal subreflector is replaced by the ellipsoidal subreflector. Revolutionary symmetrical Grogorian antennas have been designed and used for many years by Andrew Antenna Corporation. But until now, there are neither CAD nor CAA programs appeared in the open literature. Therefore, it is also useful to develop the CAD and CAA programs to design the shaped reflector Gregorian antenna for specific requirement as well as for optimization.

In this thesis, the design and analyses of Cassegrain and Gregorian antennas are carried out in detail. Corrugated conical horn is studied and shown the best choice for the dual reflector antenna feeds. The propagation and radiation characteristics are discussed in detail. On the assumption that the dimensions of reflectors are much larger than the wavelength, the geometrical optics (GO) approach is used throughout in the reflector design. The analysis programs are developed based on physical optics (PO) technique. Various performance trade-offs and comparison between Cassegrain and Gregorian antennas are carried out.

1.2 Literature Review

Reflector antennas have been used since the radio pioneering era of Lodge, Hertz, and Marconi, but it took the exigent demands of radio communications in World War II to stimulate a real development in the reflector art. Subsequent interest in the science of radio astronomy and the inception of terrestrial microwave links were responsible for a fast growth in the field, so that in the 1940's and 1950's the design principles and requirements for prime focus fed system were well established. With the advent of satellite tracking and telecommunication networks, Cassegrain, or secondary focus system, and horn reflectors came into prominence in the early 1960's. The desire to maximize the gain, or the gain-temperature ratio, has led to the development of sophisticated computer analysis techniques. For properly imposing the power illumination over the aperture of the main reflector and by shaping of both reflectors, one can minimize spillover and in turn maximize efficiency. In the application of radio astronomy and space telecommunications, many kinds of reflector antennas have been proposed and studied based on the theoretical and experimental research. One of the commonly used reflector antennas is the revolutionary symmetrical Cassegrain antenna which was considered only for those applications requiring the 3db beamwidth of less than about one degree. Today, this antenna shows even more important due to the rapid development of space communications and other applications.

The first reflector antenna was born in the year 1888 in the laboratory of Heinrich Hertz. He used it to experimentally demonstrated the existence of the electromagnetic waves that had been predicted theoretically by James Clerk Maxwell some fifteen years earlier. He launched decimeter-wave radiation from a parabolic mirror antenna fed by a dipole. The directive antennas played a major part in Hertz's system, providing him with a laboratory microwave link [1]. His work stimulated a lot of scientists toward further investigation. A. Righi did a pioneer work on microwave optics [1]. Inspired by Righi's work, Marconi conceived the idea of modulating the generator so that the intelligence could be transmitted on the radio frequency optical link and he proved to the British Post Office that his idea came true by using two Hertz-type parabolic reflectors separated by a range of four miles in 1897. It is known that the optical properties of the parabololic reflectors were always used at that time. Marconi got his first patent on the sharp beam cylindrical parabola antenna in 1896 [1]. The first hollow pipe or "waveguide" radiator were developed by Lodge in 1894 [1] and in 1897, Bose first used the pyramidal electromagnetic horn as the receiving antenna which was then called "collecting funnel" [1]. Actually, his antenna was the first flare waveguide which he would like to use to collect more energy by increasing the cross section. It should be noted that the major practical advances tended to arise from the microwave optics and these researches pointed the direction in which the new microwave radio technology must go.

In 1931, the first discovery of extra-terrestrial radio emission made the genesis of the science of radio astronomy and then in 1937, the first large paraboloidal reflector was constructed and used as a radio telescope antenna by Reber [2]. The reflector was 9.6m in diameter and the wavelength was 1.9m. In World War II, a vast and intensive development effort was the microwave physics founded on the solid base of physical optics and electromagnetic theory. This stimulated the development of the unified theory of microwave antennas which was well covered in the now classic text by Silver [3]. With the rebirth of the radio astronomy immediately after the war, many former wartime radio scientists turned their interests to develop radio telescopes and many really large reflector antennas came on. But the commonly used feed was the dipole and the limited beam steering could be achieved by displacing the feed from the focal point. The gain was only about 31db [4].

It was Cutler who first published the paper dealing with the polarization characteristics of reflector antennas [5] in 1947. He showed qualitatively that the ideal feed should radiate a spherical wave with the linear polarization and also examined the polarization characteristics of the then-popular dipole feed and stated that it would give rise to cross-polarization components in the reflected field. In his paper in 1954 [6], Jones first showed how an electric dipole and a magnetic dipole may be combined to produce a unidirectional Huygens source having ideal polarization characteristics for feeding a paraboloid. Later, Koffman also did some research on feed polarization for parallel currents in reflectors generated by conic sections [7] and drew the same conclusion as Jones.

No discussion of two reflector antennas would be complete without a reference to that family which is derived from the 17th century optical telescope devised by the Cassegrain, include variants due to Gregory and Newton. Cassegrain antennas were being experimentally developed at least as early as the mid 1950s, and the whole family has been well described by Hannan in 1961 [8]. Two reflector antenna systems have been analyzed from the point of view of geometrical optics by Kinber in 1962 [9]. Morgan gave some examples of generalized Cassegrain and Gregorian antennas [10]. They showed that the Cassegrain antenna can produce a very sharp beam and an extremely high gain for telecommunications.

Since 1960's, with the development of satellite communications, the large antennas are no longer the exclusive province of radio astronomers. Many reflector antennas were used in the commercial satellite communications earth stations and such antennas were costly. In Potter's paper [11], it was estimated that the cost of a single large reflector antenna was proportional to its diameter raised to the power 2.78. Thus it became imperative to increase the aperture efficiency and to reduce feed spillover so as to maximize the gain. In 1963, Galindo first showed that with a two-reflector system it is possible to achieve arbitrary phase and amplitude distributions over the main aperture using geometric optics [12]. In 1965, Williams described a modified Cassegrain system to which an approach was elegantly applied, leading to a improvement about 25% in aperture efficiency [13].

Its operation can be explained quite simply in terms of ray optics. Starting with a conventional Cassegrain system with prescribed feed pattern, the hyperboloidal subreflector's surface is deformed in such a way as to increase the ray density radially outward from the axis. When properly done a good approximation to a uniform amplitude distribution across the main aperture is realized, but only at the expense of a nonuniform phase distribution. However, the phase error can be corrected by a relative minor change in the main reflector surface without significantly affecting the amplitude taper.

A milestone in the development of reflector antennas was that the dipole feeds had been replaced mostly by the microwave horns in 1960's. Nevertheless the dominant mode horn's characteristics are far from ideal for this purpose, chiefly because its principal E and H plane radiation patterns are quite different. In 1963, Potter devised a clever solution to this problem in the case of the TE_{11} mode excited conical horn [14]. He noted that a step discontinuity in diameter near the throat of the horn would cause some of the dominant mode to be converted to the higher-order TM_{11} mode. He further showed that the correct combination of these two modes at the horn aperture would lead to a radiation pattern have almost identical patterns in the E and H planes, and that the normally high E plane sidelobes would be suppressed to a very low level. Then Potter and Ludwig [15] extended the concept to include additional higher modes (TE_{12}, TE_{13} and TM_{12}) in the conical horn for purposes of beam shaping and showed how to obtain a feed pattern that more nearly approximates a uniform illumination over a reflector aperture. These multimode horns are not broadband devices because the various modes propagate with different velocities. This difficulty was overcome in the corrugated horn which seems to have been conceived in the USA and in Australia almost at the same time, about 1964. In USA, Kay used grooved walls in a wide flare angle horn and called it the scalar feed because its properties were largely independent of polarization [16]. In Australia, an analytical description of the synthesis of the hybrid HE_{11} mode was given in an early paper by Minnett and Thomas [17] and they also studied the fields in the image space of symmetrical focusing reflectors and proposed the guideline on how to synthesize the high-efficiency low-noise feeds using hybrid-waves in corrugated waveguides [18]. Because the corrugated horn radiates a pattern with the polarization properties of a Huygens source, it results in a very low level of cross-polarization radiation in reflector antennas. The striking success of this horn as a feed has been an important factor leading to improved performance in reflector systems and has inspired a great deal of investigation of some scientists [19][20][21][22][23].

In the design of pencil-beam antennas for various applications, the most important parameters are: a) high efficiency, b) low cross-polarization, c) satisfactory sidelobe envelope. Many scientists have put a tromendous effort in improving these requirements. In order to achieve high efficiency, both of the two reflectors will be shaped based on the classical Cassegrain antenna to obtain the uniform aperture illumination in both phase and amplitude. Galindo first used the geometric optics technique (GO) to design the reflectors to achieve high efficiency [12]. If the antenna is large, a successful design may be undertaken using GO to satisfy increasingly stringent requirements on efficiency and radiation pattern. Indeed, these techniques are in widespread used and now form a part of the important body of antenna theory. When near maximum gain is required, the symmetrical dual reflectors such as Cassegrain and Gregorian configurations are shaped to provide an optimal solution. This technique has been extended to offset dual-reflector configurations [24][25][26]. In recent years, the GO is also widely used in the satellite antenna design [27][28] and larger earth station antenna design [29][30]. The computer aided design of the reflector antennas with the GO is a very popular topic in antenna theory and technology today. However, it must be remembered that the GO is only valid when the wavelength is much smaller compared with the dimensions of the reflectors. If significant efficiency enhancement is hoped to be obtained in all but the largest system, diffraction techniques must be used. Daveau [31] first applied scalar-diffraction theory to scattering by the sub reflector in order to design for an optimum illumination pattern. The phase may then be equalized by small changes in the main reflector profile. This approach was a direct extension of GO analysis of Green [32]. P.D. Potter used a phase-matching criterion to obtain the sub reflector shape based on the application of spherical wave theory to Cassgrainian-fed paraboloids [33]. A significant advance, enabling direct optimization of efficiency to be undertaken, was made by Wood [34][35][36]. In his approach, using a method based on reciprocity, a concise expression for efficiency is obtained which only involves an integration over the sub reflector surface. Several other authors [37][38] [39] also successfully used the GTD techniques to modify GO to design the reflector antennas.

The most significant cause of the cross-polarization is the fact that feed $E-$plane and $H-$plane patterns are not identical. In addition to the feed, the scattering from the struts used to keep the feed or subreflector in position is another reason for cross-polarization. For two-reflector case the dielectric cone feed suggested by

Bartlett and Mosely [40] and later developed by Clarricoats and Salema [41] was a effective way to reduce the cross-polarization. And the offset reflector antennas fed by carefully designed feed have become widespread to eliminate the struts scattering [42].

According to the current CCITT recommendations for earth station antennas, the close-in and the far-angle sidelobes should meet the specification to minimize possible interferences with other communication systems, especially in areas of population concentration. The overall pattern control becomes one of the major antenna design issues. The near-in sidelobes depend mainly on the amplitude taper at the edge of the main reflector and the central blockage. In 1960, Taylor first proposed the Taylor aperture distribution and used it to investigate the beamwidth and the sidelobes [43]. Later, Hansen [44], Ludwig [45] also published their papers on how to reduce the reflector antenna sidelobes based on the studies on the aperture amplitude distributions. Recently, the Gaussian distribution and a generalized three-parameter aperture distribution were used by Galindo [30] and Duan [46] to improve the radiation characteristics. The far-angle sidelobes of the two-reflector antennas mainly come from the feed spillover past the subreflector and the subreflector rim diffraction, main reflector spillover and diffraction, energy scattered from the feed after reflection. The subreflector and main reflector spillovers may be reduced by increasing the edge tapers, but the antenna efficiency will be decreased. Properly selecting the edge tapers and shaping the reflector profiles are very important in the antenna design, as stated by Clarricoats and Poulton [47].

On the evaluation of the performance of the reflector antennas, the radiation patterns are normally considered by using the methods known as asymptotic solutions of Maxwell's equations explained by Kouyoumjian [48]. These studies may be divided into three classes. The first is the geometrical optics (GO), in which the propagation of electromagnetic energy takes place along the ray. Laws of optics such as energy conservation, Fermat's principle, Fresnel laws etc. are used [49]. The second is the geometrical optics theory of diffraction (GTD), which is an extension of the GO by the introduction of diffracted rays because GO is not valid at the edges or in the shadow of a reflector. Keller [50] was the first who introduced this theory, later improved by Kouyoumjian [51]. The third is physical optics (PO) approximation, which has been used by a great number of scientists such as Kinber [52], Rusch [53], and Shogen [28]. The radiation properties of any reflector can be calculated directly from the electric currents which are physically responsible for initiating the radiation. It is shown that PO is valid in calculating the radiation patterns even if the diameter of the reflector is only several wavelengths [54]. The PO is almost always recommended for use in calculating the radiation patterns of the dual reflector antennas used in satellite communications. The work has been done by Rusch and Potter [55], but there is still limitation in their analysis. Nevertheless, both the scattering pattrens of the subreflector and the radiation patterns can be obtained with PO and then the entire antenna performance can be predicted.

1.3 Scope of the Work

In this thesis, two kinds of revolutionary symmetric reflector antennas, Cassegrain and Gregorian antennas which are mostly used in satellite communication earth stations will be studied in detail. The research is concentrated on the following topics:

(1) The antenna feeds will be analyzed and designed to produce high-efficiency pencil-beam. The requirements of feeds used in Cassegrain and Gregorian antennas will be descussed and the feed selection will be given.

(2) The computer-aided synthesis of subreflector and main reflector will be carried out based on the geometric optics (GO) approach. Using the calculated or measured feed radiation patterns and the desired main reflector aperture power illumination, GO can be employed to obtain a set of differential equations related to the surface profiles of subreflector and main reflector, then these differential equations can in turn be solved by numerical methods to obtain the reflector profiles.

(3) Once the profiles of subreflector and main reflector are known, the physical optics (PO) will be used to evaluate the scattered patterns of the subreflector and the radiation patterns of the main reflector. The whole antenna performance, such as aperture efficiency, boresight gain, sidelobes and beamwidth are predicted.

(4) Various power distributions will be imposed on the main reflector aperture to investigate the trade-offs between antenna gain and sidelobes. Comparison between Cassegrain antenna and Gregorian antenna will be made.

1.4 Organization of the Thesis

This thesis is organized as follows:

Chapter 2 presents high performance antenna feeds.

Chapter 3 briefly introduces the dual reflector antenna configrations and in detail the reflector profile synthesis method with GO.

Chapter 4 reports on the implementation of PO to calculate the subreflector scattered patterns and the main reflector radiation patterns of Cassegrain antennas and Gregorian antennas.

Chapter 5 contains a brief discussion of trade-offs between the aperture illumination and the performance. The performances of the Cassegrain antennas and the Gregorian antennas are compared.

Chapter 6 gives the conclusion and the recommendations for future work.

Chapter 2

High-Performance Antenna Feeds

In pencil beam antenna designs, major efforts have been concentrated on the design of feeds which can efficiently illuminate the reflectors so that the antenna performance can be greatly increased. For example, the antenna efficiency is closely related to the feed characteristics factors; such as the unsymmetric feed radiation patterns introduce the undefined phase centers, cause cross-polarization fields and may create the non-uniform aperture illuminations and spillover losses. Hence, a proper feed design plays a very important role in the antenna design.

The selection of feeds that are most suitable for reflector antennas was always a major research topic. H.C. Minnet and B.M. Thomas were the first ones who investigated the field distribution in the focal plane of the paraboloidal reflector based on the Maxwell's equations [17][18]. Using only the induced primary surface current due to an incident plane wave field, they showed that the fields in the focal plane can be represented by a spectrum of hybrid waves that are simply linear combination of TE and TM modes and, when satisfying some special waveguide boundary conditions, these hybrid modes can exist in the waveguide. This research was the theoretical foundation of the development of corrugated waveguides and corrugated conical horns.

2.1 Corrugated waveguide feeds

The corrugated waveguide structure is shown in Figures 2.1a, b, c. The analyses given in this section will be extended to the corrugated conical horns.

2.1.1 Propagation Characteristics

(a) Field Components:

Based on the Maxwell's equations, it can be shown that the longitudinal components, i.e. E_z and H_z of transverse electric and magnetic fields in the homogeneous waveguide satisfy the Helmholtz equations respectively:

$$[\nabla_t^2 + (k^2 - \beta^2)]E_z = 0$$
$$[\nabla_t^2 + (k^2 - \beta^2)]H_z = 0$$

where $\beta = 2\pi/\lambda$, the propagation constant in the lossless medium, λ is wavelength. $k^2 = \omega^2\mu_0\epsilon_0$, k is the free space wave number, ω is angular frequency, μ_0 and ϵ_0 are free space permeability and permittivity. When both E_z and H_z are known, then the transverse fields in cylindrical coordinates (r, ψ, z) are given by

$$E_r = -\frac{j}{k^2 - \beta^2}(\beta\frac{\partial E_z}{\partial r} + \frac{\omega\mu_0}{r}\frac{\partial H_z}{\partial\psi}) \tag{2.1}$$

$$E_\psi = \frac{j}{k^2 - \beta^2}(-\frac{\beta}{r}\frac{\partial E_z}{\partial\psi} + \omega\mu_0\frac{\partial H_z}{\partial r}) \tag{2.2}$$

$$H_r = \frac{j}{k^2 - \beta^2}(\frac{\omega\epsilon_0}{r}\frac{\partial E_z}{\partial\psi} - \beta\frac{\partial H_z}{\partial r}) \tag{2.3}$$

$$H_\psi = -\frac{j}{k^2 - \beta^2}(\omega\epsilon_0\frac{\partial E_z}{\partial r} + \frac{\beta}{r}\frac{\partial H_z}{\partial\psi}) \tag{2.4}$$

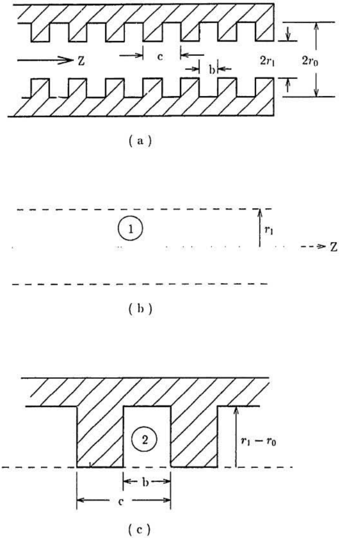

Figure 2.1: Corrugated waveguide feed. (a) Structure. (b) Region 1. (c) Region 2.

In region 1 ($r < r_1$), E_z and H_z are given by:

$$E_z = a_m J_m(x) e^{jm\psi} e^{-j\beta z} \tag{2.5}$$

$$H_z = -a_m j Y_0 \Gamma J_m(x) e^{jm\psi} e^{-j\beta z} \tag{2.6}$$

where $x = Kr, K^2 = k^2 - \beta^2, Y_0 = 1/Z_0 = \sqrt{\frac{\epsilon_0}{\mu_0}}, \Gamma = -\frac{1}{jY_0}\frac{H_z}{E_z}$. In order to satisfy the boundary condition that the fields at $r = 0$ are finite, the Bessel function of the 1st kind is used for in E_z and H_z. Using eqs.(2.1)-(2.6), the transverse field components can be obtained:

$$E_r = -a_m j \frac{k}{K} \frac{J_m(x)}{x} [\bar{\beta} F_m(x) + m\Gamma] e^{jm\psi} \tag{2.7}$$

$$E_\psi = a_m \frac{k}{K} \frac{J_m(x)}{x} [m\bar{\beta} + \Gamma F_m(x)] e^{jm\psi} \tag{2.8}$$

$$H_r = -a_m \frac{k}{K} Y_0 \frac{J_m(x)}{x} [\bar{\beta} \Gamma F_m(x) + m] e^{jm\psi} \tag{2.9}$$

$$H_\psi = -a_m j \frac{k}{K} Y_0 \frac{J_m(x)}{x} [m\bar{\beta}\Gamma + F_m(x)] e^{jm\psi} \tag{2.10}$$

where $\bar{\beta} = \frac{\beta}{k}, F_m(x) = x\frac{J_m'(x)}{J_m(x)}$. In eqs.(2.7)-(2.10), the factor $e^{j(\omega t - \beta z)}$ is understood throughout.

In region 2 ($r_1 < r < r_0$), as shown in Figure 2.1(c), if the waveguide wall is perfectly conducting, we consider that only TM modes in this region exist, i.e. $H_z = 0$, then E_z must exist and $\frac{\partial E_z}{\partial r} = 0$ and $\frac{\partial E_z}{\partial \psi} = 0$ because $\hat{n} \cdot \vec{B} = 0$ at the perfectly conducting wall. In addition, if the slot is relatively short with respect to the wavelength, the TM modes are assumed to be z-independent. That means β tends to 0. These modes are not the propagation modes. Hence, E_z can be expressed as:

$$E_z = \frac{a_m'}{Y_m(x_0')}[J_m(x')Y_m(x_0') - Y_m(x')J_m(x_0')]e^{jm\psi}$$

which satisfies the boundary condition at the waveguide wall, $r = r_0$, $E_z = 0$, where $x' = kx$. Eqs.(2.1)-(2.4) are used to obtain other field components in this region. But what we are really interested in is H_ψ which will be used in the following admittance matching technique. H_ψ can be expressed as:

$$H_\psi = -jY_0 \frac{a_m'}{Y_m(x_0')}[J_m'(x')Y_m(x_0') - Y_m'(x')J_m(x_0')]e^{jm\psi}$$

(b) Radial Field Admittance Matching Technique at $r = r_1$:

First, because the transverse electric (TE) modes in the slots do not exit, it is reasonable to assume $E_\psi = 0$ at $r = r_1$, so that the TE modes can not be supported in the slots. Then from the fields in region 1, we have

$$m\bar{\beta} = -\Gamma F_m(x_1) \tag{2.11}$$

At $r = r_1$, the admittance in the radial direction H_ψ / E_z should be same in both regions. Using the field expressions above, we can get

$$F_m(x_1) - \frac{(m\bar{\beta})^2}{F_m(x_1)} = (\frac{k}{K})^2 S_m(x_1', x_0') \tag{2.12}$$

where

$$S_m(x, y) = x\frac{J_m'(x)Y_m(y) - J_m(y)Y_m'(x)}{J_m(x)Y_m(y) - J_m(y)Y_m(x)} \tag{2.13}$$

The eq.(2.12) is called the characteristic equation of $\bar{\beta}$. It treats the boundary at $r = r_1$ as if it is a continuous impedance surface.

(c) Balanced-Hybrid Condition:

For a given mode, the pass-band for propagation has lower and upper frequency limits given by

$$\bar{\beta} = 0 \rightarrow F_m(x_1) = S_m(x_1', x_0')$$
$$\bar{\beta} = \infty \rightarrow S_m(x_1', x_0') = 0$$

When $\bar{\beta} = \infty$ for cutoff modes, x_1 satisfies the condition $S_m(x_1', x_0') = 0$, but the other propagation modes exhibits special characteristic from eq.(2.12), that is

$$F_m(x_1) = \pm m\bar{\beta}$$

Refer to eq.(2.11), we have

$$\Gamma = \mp 1 \tag{2.14}$$

This is called the balanced-hybrid condition, where + sign refer to the HE mode and − sign refer to EH mode.

(d) HE_{11} modes:

Let $m = 1$, from eqs.(2.5)-(2.10) we can express the HE_{1m} mode fields in the linearly polarized form as:

$$E_z = a_1 J_1(x)\cos\psi \tag{2.15}$$

$$H_z = a_1 Y_0 \Gamma J_1(x)\sin\psi \tag{2.16}$$

$$E_r = -ja_1\frac{k}{K}[\bar{\beta}J_1(x) + \Gamma\frac{J_1(x)}{x}]\cos\psi \tag{2.17}$$

$$E_\psi = ja_1\frac{k}{K}[\bar{\beta}\frac{J_1(x)}{x} + \Gamma J_1'(x)]\sin\psi \tag{2.18}$$

$$H_r = -ja_1 Y_0\frac{k}{K}[\bar{\beta}\Gamma J_1'(x) + \frac{J_1(x)}{x}]\sin\psi \tag{2.19}$$

$$H_\psi = -ja_1 Y_0\frac{k}{K}[\bar{\beta}\Gamma\frac{J_1(x)}{x} + J_1'(x)]\cos\psi \tag{2.20}$$

For E fields, use

$$\begin{bmatrix} E_x \\ E_y \end{bmatrix} = \begin{bmatrix} \cos\psi & -\sin\psi \\ \sin\psi & \cos\psi \end{bmatrix}\begin{bmatrix} E_r \\ E_\psi \end{bmatrix}$$

we can obtain:

$$E_x = -\frac{1}{2}ja_1\frac{k}{K}[(\bar{\beta}+\Gamma)J_0(x) + (\Gamma-\bar{\beta})J_2(x)\cos 2\psi] \tag{2.21}$$

$$E_y = -\frac{1}{2} j a_1 \frac{k}{K} (\Gamma - \bar{\beta}) J_2(x) \sin 2\psi \tag{2.22}$$

In the balanced-hybrid condition for HE_{11} mode, $\Gamma = +1$. If the radius r_1 is large enough so that $kr \gg 1$, then $\bar{\beta} \to 1$ and $E_y = 0$. This is the HE_{11} mode's linearly polarization situation. On the other hand, since the longitudinal components of electric and magnetic fields of HE_{11} mode are in the ratio of free space wave impedance, it can be predict that the radiation pattern of the waveguide exhibits symmetry and zero cross-polarization.

In the waveguide structure, when r_1/λ is large, $S_1(x_1', x_0') \to x_1' \cot(x_0' - x_1')$, on the balanced-hybrid condition $S_1 = 0$, so the slot depth is nearly $r_0 - r_1 = \lambda/4$.

2.1.2 Radiation Characteristics

For the HE_{11} mode, to obtain the radiation pattern of an open-ended corrugated waveguide, the Kirchhoff-Huygen integration[3] over the aperture field in the region $r < r_1$, assuming all fields to vanish for $r > r_1$, is used. Refer to Figure 2.2, the electric radiation field can be expressed as:

$$E_p(R', \theta', \phi') = \frac{jke^{-jkR'}}{4\pi R'} \vec{i}_{R'} \times \int_{aperture} \{\vec{i}_n \times \vec{E}_t - Z_0 \vec{i}_{R'} \times (\vec{i}_n \times \vec{H}_t)\} e^{jk\vec{r}\cdot\vec{i}_{R'}} dS \tag{2.23}$$

Using the field expression in HE_{11} mode, it can be shown that the fields HE_{11} are given as follows:

$$E_{p\theta}(\theta', \phi') = F(\theta') \frac{akr_1}{2KR'} e^{-jkR'} \cos\phi' \tag{2.24}$$

$$E_{p\phi}(\theta', \phi') = -F(\theta') \frac{akr_1}{2KR'} e^{-jkR'} \sin\phi' \tag{2.25}$$

where

$$F(\theta') = L(\theta')(1 + \bar{\beta}\cos\theta') + Q(\theta')(\cos\theta' + \bar{\beta}) \tag{2.26}$$

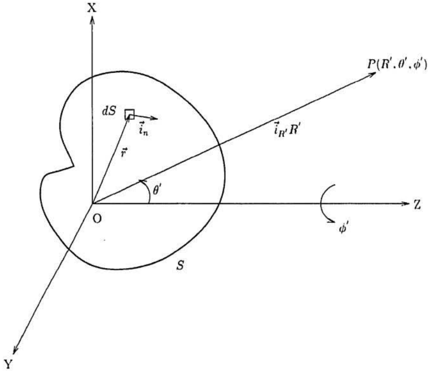

Figure 2.2: Co-ordinate system used for evaluating the Kirchhoff-Huygen integration.

$$L(\theta) = \frac{J_1(u_1)J_1(x_1)}{u_1 x_1} \tag{2.27}$$

$$Q(\theta) = \frac{x_1 J_1(x_1)J_1'(u_1) - u_1 J_1(u_1)J_1'(x_1)}{x_1^2 - u_1^2} \tag{2.28}$$

where $u_1 = x_1' \sin\theta', x_1 = Kr_1$, $\bar{\beta}$ can be calculated from $\bar{\beta} = F_1(x_1)$.

In E-plane ($\phi' = \frac{\pi}{2}$), $E_{p\theta} = F(\theta')\frac{akr_1}{2KR'}e^{-jkR'}$,

in H-plane ($\phi' = 0$), $E_{p\phi} = F(\theta')\frac{akr_1}{2KR'}e^{-jkR'}$, the E-plane and H-plane pattern are identical.

Since

$$E_x = E_\theta(\theta', \phi')\cos\phi' - E_\phi(\theta', \phi')\sin\phi'$$

$$E_y = E_\theta(\theta', \phi')\sin\phi' + E_\phi(\theta', \phi')\cos\phi'$$

it follows that there are no crosspolarized components in the radiation field if the field in the aperture is linearly polarized.

2.2 Corrugated Conical Horn Feeds

Clarricoats [23] [47] shows that HE_{11} mode corrugated waveguide feeds are not generally suitable for the Cassegrain antennas because their beamwidths are too broad. If we want to use a narrow beamwidth circularly symmetric radiation pattern to illuminate the subreflector, the corrugated conical horn is a favorable choice. Although corrugated waveguides have found rather limited application as feeds for large reflector antennas, the method of analysis provides substantial insight into the design of corrugated conical horns.

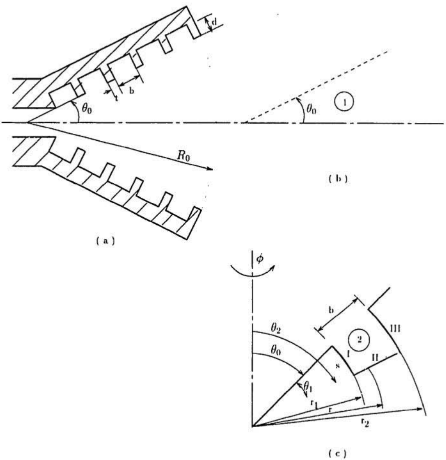

Figure 2.3: Corrugated conical horn. (a) Structure. (b) Region 1. (c) Region 2.

2.2.1 Propagation Characteristics

The structure of the corrugated conical horn is shown in Figure 2.3(a). If the half flare angle does not exceed about 5°, the cylindrical mode analysis of the corrugated waveguide feed presented above may be applied directly to these horns. For the large angle, it is usually more convenient to analyze this kind of horn based on spherical hybrid modes and we also use the impedance matching technique on the boundary between region 1 and region 2, as shown in Figure 2.3b and Figure 2.3c respectively.

(a) Fields Expressions:

The modes in the conical horn can be derived from the vector potentials $\vec{A}$ and $\vec{F}$, given by

$$\vec{A} = \vec{a}_r A_r$$

$$\vec{F} = \vec{a}_r F_r$$

where $\vec{a}_r$ is the unit vector in r direction. The fields expressed by $\vec{A}$ and $\vec{F}$ are given by

$$\vec{E} = -\nabla \times \vec{F} + \frac{1}{j\omega\epsilon_0} \nabla \times \nabla \times \vec{A} \tag{2.29}$$

$$\vec{H} = \nabla \times \vec{A} + \frac{1}{j\omega\mu_0} \nabla \times \nabla \times \vec{F} \tag{2.30}$$

A_r and F_r satisfy Helmholtz equation:

$$\nabla^2 A_r + k^2 A_r = 0 \tag{2.31}$$

$$\nabla^2 F_r + k^2 F_r = 0 \tag{2.32}$$

In a spherical coordinate system (r, θ, ϕ), we define the fields corresponding to $\vec{A}$ are called TM modes and that corresponding to $\vec{F}$ are called TE modes. So for

TM modes, the field expressions are:

$$E_r = \frac{1}{j\omega\epsilon_0}(\frac{\partial^2}{\partial r^2} + k^2)A_r \tag{2.33}$$

$$E_\theta = \frac{1}{j\omega\epsilon_0}\frac{1}{r}\frac{\partial^2 A_r}{\partial r\partial\theta} \tag{2.34}$$

$$E_\phi = \frac{1}{j\omega\epsilon_0}\frac{1}{r\sin\theta}\frac{\partial^2 Ar}{\partial r\partial\phi} \tag{2.35}$$

$$H_r = 0 \tag{2.36}$$

$$H_\theta = \frac{1}{r\sin\theta}\frac{\partial A_r}{\partial\phi} \tag{2.37}$$

$$H_\phi = -\frac{1}{r}\frac{\partial A_r}{\partial\theta} \tag{2.38}$$

For TE modes, the field expressions are:

$$E_r = 0 \tag{2.39}$$

$$E_\theta = -\frac{1}{r\sin\theta}\frac{\partial F_r}{\partial\phi} \tag{2.40}$$

$$E_\phi = \frac{1}{r}\frac{\partial F_r}{\partial\theta} \tag{2.41}$$

$$H_r = \frac{1}{j\omega\mu_0}(\frac{\partial^2}{\partial r^2} + k^2)F_r \tag{2.42}$$

$$H_\theta = \frac{1}{j\omega\mu_0}\frac{1}{r}\frac{\partial^2 F_r}{\partial r\partial\theta} \tag{2.43}$$

$$H_\phi = \frac{1}{j\omega\mu_0}\frac{1}{r\sin\theta}\frac{\partial^2 F_r}{\partial r\partial\phi} \tag{2.44}$$

For the hybrid mode, the fields are the combination of TM and TE modes.

In spherical coordinate system, the solutions for the Helmholtz eq(31)-(32) can be obtained by the method of separation of variables.

In region 1 ($-\theta_0 < \theta < \theta_0$), the hybrid mode exists. If $kr \gg 1$, the radiation condition should be satisfied, we have:

$$A_r = Akrh_n^{(2)}(kr)P_n^m(\cos\theta)e^{jm\phi} \tag{2.45}$$

$$F_r = Bkrh_n^{(2)}(kr)P_n^m(\cos\theta)e^{jm\phi} \tag{2.46}$$

The coefficients A and B are defined by the relation $B/A = -jZ_0\Gamma$, $Z_0 = \sqrt{\frac{\mu_0}{\epsilon_0}}$. In eq.(2.45) and (2.46) $Q_n^m(\cos\theta)$ is omitted because $\theta = 0$ is included. In the above two equations, $h_n^{(2)}(kr)$ is a spherical Hankel function of the 2nd kind. $P_n^m(\cos\theta)$ and $Q_n^m(\cos\theta)$ are the associated Legendre function of the first kind and the second kind, respectively.

The field components can be obtained from eqs.(2.33)-(2.44). For convenience, let $\hat{H}_n = krh_n^{(2)}(kr)$, $P_n^m(\cos\theta) = P_n^m$ and $e^{jm\phi}$ is understood.

$$E_r = AZ_0n\frac{n+1}{jkr^2}\hat{H}_nP_n^m \tag{2.47}$$

$$H_r = -A\Gamma n\frac{n+1}{kr^2}\hat{H}_nP_n^m \tag{2.48}$$

$$E_\theta = -Z_0A(\frac{m\Gamma}{r\sin\theta}\hat{H}_nP_n^m + \frac{j}{r}\hat{H}_n\frac{dP_n^m}{d\theta}) \tag{2.49}$$

$$E_\phi = Z_0A(-\frac{j\Gamma}{r}\hat{H}_n\frac{dP_n^m}{d\theta} + \frac{m}{r\sin\theta}\hat{H}'_nP_n^m) \tag{2.50}$$

$$H_\theta = A(\frac{jm\hat{H}_n}{r\sin\theta}P_n^m - \Gamma\frac{\hat{H}'_n}{r}\frac{dP_n^m}{d\theta}) \tag{2.51}$$

$$H_\phi = -A(\frac{\hat{H}_n}{r}\frac{dP_n^m}{d\theta} + j\frac{\Gamma m\hat{H}'_n}{r\sin\theta}P_n^m) \tag{2.52}$$

In region 2, the grooves in the feed are perpendicular to the wall of the horn, as shown in Figure 2.3(a), the computation of the fields is very difficult because the boundaries do not coincide with the spherical coordinate. Therefore, for a groove not too close to the apex of the horn, it is assumed to be the one shown in Figure 2.3(c). It is also assumed that only TM modes can exist in the groove. So only A_r is used to give the field expressions. We have:

$$A_r = kr[a_n J_n(kr)+b_n Y_n(kr)]\times[c_{nm} P_n^m(\cos\theta)+d_n^m Q_n^m(\cos\theta)]\times[c_m \cos m\phi+f_m \sin m\phi] \tag{2.53}$$

From the boundary conditions: $E_\phi = 0$ at $r = r_1$ and $r = r_2$, we have:

$$\begin{vmatrix} J_n(kr_1) + kr_1 J_n'(kr_1) & Y_n(kr_1) + kr_1 Y_n'(kr_1) \\ J_n(kr_2) + kr_2 J_n'(kr_2) & Y_n(kr_2) + kr_2 Y_n'(kr_2) \end{vmatrix} = 0 \tag{2.54}$$

If this equation has solutions, then TM modes exist. Using the boundary conditions: $E_\phi = 0$ and $E_r = 0$ at $\theta = \theta_2$, we can get A_r in the form of:

$$A_r = kr[Y_n(kr_1) + kr_1 Y_n'(kr_1)]J_n(kr) - [J_n(kr_1 + kr_1 J_n'(kr_1)]Y_n(kr)$$

$$\times[Q_n^m(\cos\theta_2)P_n^m(\cos\theta) - P_n^m(\cos\theta_2)Q_n^m(\cos\theta)]$$

$$\times\ (e_m \cos m\phi + f_m \sin m\phi) \tag{2.55}$$

Now let's consider eq.(2.54) to derive the condition for TM mode existance. We use

$$f_n'(x) = \tfrac{n}{x} f_n(x) - f_{n+1}(x) = f_{n-1}(x) - \tfrac{n+1}{x} f_n(x)$$
$$f_n(x+h) = f_n(x) + h f_n'(x) +^{\circ} (h^2)$$

where $f_n(x)$ stands for $J_n(x)$ and $Y_n(x)$. we also assume $kb = k(r_2 - r_1) \ll 1$ and $kr_1 \gg 1$, then from eq.(2.54), we can obtain [56]:

$$n = -\tfrac{1}{2} + [\tfrac{1}{4} + (kr_1)^2]^{0.5} \approx kr_1$$

So the TM modes do exist even if the groove width is very small.

(b) Field Impedance Matching Technique at $\theta = \theta_0$:

In region 2, suppose there are many grooves in one λ and we formulate the boundary conditions at $\theta = \theta_0$ in terms of two impedance Z_ϕ and Z_r defined by:

$$E_\phi = Z_\phi H_r, \quad E_r = Z_r H_\phi$$

From the *TM* field expressions in this region, under the conditions $kr \gg 1$, $kb \ll 1$, i.e., the grooves are far away from apex and the groove width is much smaller than λ, then we have

$$Z_\phi = 0 \tag{2.56}$$

$$Z_r \approx -jZ_0 \tan(ks) \tag{2.57}$$

s is defined in Figure 2.3(c). When $s \to \lambda/4, Z_r \to \infty$.

In region 1, in order to support only the *TM* modes in the grooves, the boundary impedances at $\theta = \theta_0$ must be the same as those in region 2. From eqs.(2.47)-(2.52), we have

$$Z_\phi = \frac{E_\phi}{H_r} = \frac{jkrZ_0}{n(n+1)}[p_n^m(\theta) + \frac{jmh_n}{\Gamma \sin\theta}] \tag{2.58}$$

$$Z_r = \frac{H_\phi}{E_r} = -\frac{jkrY_0}{n(n+1)}[p_n^m(\theta) + \frac{j\Gamma m h_n}{\sin\theta}] \tag{2.59}$$

where

$$p_n^m = \frac{dP_n^m(\cos\theta)}{d\theta} / P_n^m(\cos\theta) \tag{2.60}$$

$$h_n = \frac{H_n'(kr)}{H_n(kr)} \tag{2.61}$$

If the fields we are interested in are far away from the apex, i.e., $kr \gg 1$, then $h_n \to -j$. Imposing the impedance matching technique, we have

$$\Gamma = \frac{-m}{p_n^m(\theta_0)\sin\theta_0} \tag{2.62}$$

$$\Gamma = -(p_n^m(\theta_0) + \bar{Y})\frac{\sin\theta_0}{m} \tag{2.63}$$

where

$$\bar{Y} = \frac{-j}{Z_r Y_0}\frac{n(n+1)}{kr} \tag{2.64}$$

(c) Balanced-Hybrid Condition:

If in eq.(2.57), we choose $s = \lambda/4$, then $\bar{Y} = 0$. From eq.(2 62) and eq.(2.63), we obtain:

$$\Gamma = \pm 1 \tag{2.65}$$

This is called balanced-hybrid condition. The + sign refers to HE modes and - sign refers to the EH modes. Under this condition, the field components E_r and H_r are then in the ratio of free space impedance.

(d) HE_{1m} mode:

If $m = 1$ under balanced-hybrid condition with $\Gamma = +1$, from eq.(2.62), introducing a function f_n^1, we can get the characteristic equation of HE_{1m} modes as:

$$f_n^1 = \frac{dP_n^1(\cos\theta_0)}{d\theta_0} + \frac{P_n^1(\cos\theta_0)}{\sin\theta_0} = 0 \tag{2.66}$$

In eq.(2.66), n can be determined and the first root corresponds to HE_{11} mode. In the meantime, using eqs.(2.49)-(2.52), we have the field expressions for HE_{1m} modes as:

$$E_\theta = -Z_0\frac{A\hat{H}_n}{r}(\frac{P_n^1}{\sin\theta} + \frac{dP_n^1}{d\theta})\cos\phi \tag{2.67}$$

$$E_\phi = Z_0\frac{A\hat{H}_n}{r}(\frac{P_n^1}{\sin\theta} + \frac{dP_n^1}{d\theta})\sin\phi \tag{2.68}$$

$$H_\theta = -Y_0 E_\phi \tag{2.69}$$

$$H_\phi = Y_0 E_\theta \tag{2.70}$$

2.2.2 Radiation Characteristics

For HE_{1m} modes, the field expressions as stated in eqs (2.67)-(2.70) at the surface, $r = R_0$ shown in Figure 2.3(a) are known. According to Figure 2.2, the radiation field $\vec{E}_p$ can be determined by Kirchhoff-Huygen integration over the aperture bounded by $r = R_0, -\theta_1 < \theta < \theta_1, 0 < \phi < 2\pi$:

$$E_p(R',\theta',\phi') = \frac{jke^{-jkR'}}{4\pi R'}\vec{i}_{R'} \times \int_{aperture} \{\vec{i}_n \times \vec{E}_t - Z_0\vec{i}_{R'} \times (\vec{i}_n \times \vec{H}_t)\} e^{jk\vec{r}\cdot\vec{i}_{R'}} dS \tag{2.71}$$

where $\vec{i}_{R'}, \vec{i}_n$ are unit vectors, and $\vec{H}_t, \vec{E}_t$ are tangential fields to the surface of $r = R_0$, as shown in Figure 2.3(a). The final radiation fields of HE_{1m} mode can be obtained as:

$$E_{p\theta}(\theta',\phi') = [F_r(\theta') + jF_i(\theta')]\cos\phi' \tag{2.72}$$

$$E_{p\phi}(\theta',\phi') = -[F_r(\theta') + jF_i(\theta')]\sin\phi' \tag{2.73}$$

where

$$F_{\substack{r\\i}}(\theta') = D\frac{e^{-jkR'}}{R'}\int_0^{\theta_0} f_n^1(\theta)G_{\substack{r\\i}}(\theta,\theta')d\theta \tag{2.74}$$

$$\begin{aligned} G_{\substack{r\\i}} &= [(1+\cos\theta)(1+\cos\theta')\sin\theta \substack{\cos\\\sin}(a\cos\theta)J_0(b\sin\theta)] \\ &-[(1-\cos\theta)(1-\cos\theta')\sin\theta \substack{\cos\\\sin}(a\cos\theta)J_2(b\sin\theta)] \\ &\mp[2\sin\theta'\sin^2\theta \substack{\sin\\\cos} J_1(b\sin\theta)] \end{aligned}$$

where $a = kR_0\cos\theta', b = kr_0\sin\theta'$, D is a constant independent of R', θ', ϕ'.

It can be seen that the E-plane and H-plane pattern are identical and there is no crosspolarized components in the radiation field when the aperture field is linearly polarized.

2.2.3 Radiation Pattern

Obviously, the expressions for the radiated field in eqs.(2.72)-(2.74) are so complicated that they are not quite suitable for the computer analyses. Using the separation of variables, B.V.Rao [57] has simplified the Helmholtz equation in spherical coordinate system and the results are given here:

$$\frac{1}{\Theta \sin\theta}\frac{\partial}{\partial\theta}(\sin\theta\frac{\partial\Theta}{\partial\theta}) + n(n+1) - \frac{m^2}{\sin^2\theta} = 0 \qquad (2.75)$$

This equation can be further approximated by replacing $\sin\theta$ by θ for $\theta < 30^\circ$, resulting in:

$$\frac{\partial^2\Theta}{\partial v^2} + \frac{1}{v}\frac{\partial\Theta}{\partial v} + (1 - \frac{m^2}{v^2})\Theta = 0 \qquad (2.76)$$

which has the solution of $\Theta = D_m J_m(v)$. $v = \sqrt{n(n+1)} \cdot \theta$.

Then follow the same procedure described above and express the tangential electric field on the circular aperture on the horn for HE_{11} mode:

$$\vec{E}_t \approx E_0 J_0(\frac{2.405}{a}\rho) e^{-ju\rho^2} e^{j\psi} (\vec{\rho} + j\vec{\psi}) \qquad (2.77)$$

where $\vec{\rho}, \vec{\psi}$ are the unit vectors at a point $P(\rho, \psi)$ on the circular aperture of the horn expressed in cylindrical coordinate system, $u = L\pi/\lambda_0$, L is the axial length of the horn, E_0 is a constant. Using the vector diffraction formula [3], the radiation electric field can be obtained:

$$\vec{E}_s(\vec{P}) = C(1 + \cos\theta)(\vec{\theta} + j\vec{\phi}) M e^{j\phi} \qquad (2.78)$$

where

$$M = \int_0^1 J_0(2.405r) J_0(\alpha r) e^{-jvr^2} r dr \qquad (2.79)$$

and $\alpha = 2\pi a \sin\theta/\lambda_0 . r = \rho/a . v = \pi a^2/(\lambda_0 L), a$ is the aperture radius. If the aperture field is linearly polarized, then

$$\vec{E}_{s\theta}(\vec{P}) = C(1+\cos\theta)M\cos\phi\vec{\theta}$$
$$\vec{E}_{s\phi}(\vec{P}) = -C(1+\cos\theta)M\sin\phi\vec{\phi}$$

The radiated fields are linearly polarized. This far field expression is only valid for $\theta_0 < 30^o$. It can meet the requirement of engineering design of Cassegrain antennas.

2.3 Numerical Results

Based on the analyses above, especially the approximated radiation patterns given in *Sec.2.2.3*, a computer analysis program has been written. The computed results are shown in Figure 2.4 - Figure 2.6. The E-plane and H-plane patterns are identical. Several cases are given by varying the flare angle (fixed aperture radius in Figure 2.4 and fixed axial length in Figure 2.6) or changing the aperture radius (fixed flare angle in Figure 2.5). It can be seen from Figure 2.6 that, when the flare angle is very small, i.e., the horn can be taken as the corrugated waveguide, the beamwidth is very wide and the corrugated waveguide can not be of practical use in super gain antennas. Proper choice of the dimensions of the corrugated conical horn will lead to the desired horn radiation patterns.

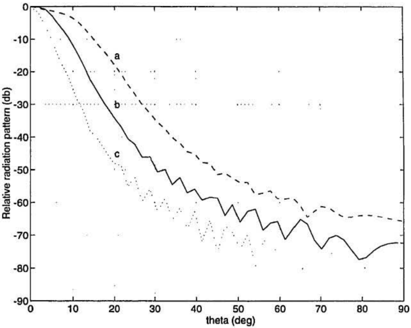

Figure 2.4: Radiation patterns of the corrugated conical horn. Frequency: 14.25GHz, Aperture radius: 8.0*in*. (a) Flare angle: 20°, (b) Flare angle: 12°, (c) Flare angle: 7°

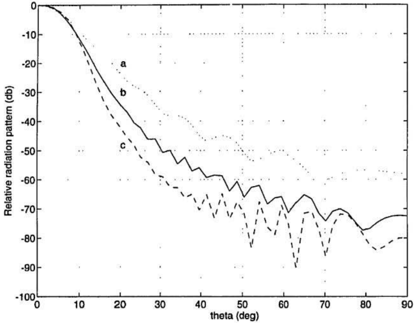

Figure 2.5: Radiation patterns of the corrugated conical horn. Frequency: 14.25GHz, Flare angle: 12°. (a) Aperture radius: 4.0*in*, (b) Aperture radius: 8.0*in*, (c) Aperture radius: 16.0*in*.

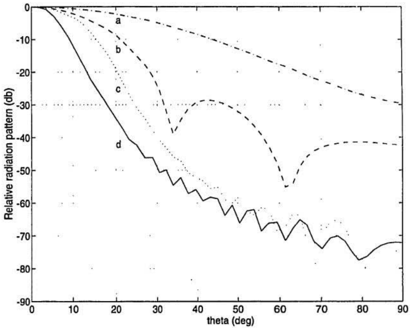

Figure 2.6: Radiation patterns of the corrugated conical horn. Frequency: 14.25GHz. Axial length: 37.0*in*. (a) Flare Angle: 1°, (b) Flare Angle: 2°, (c) Flare Angle: 20°, (d) Flare Angle: 12°

Chapter 3

Dual Shaped Reflector Antenna Design

The rotationally symmetrical dual shaped reflector antennas used in earth stations are described. The classical Cassegrain and Gregorian antennas have a low efficiency due to the fact that the aperture illumination can not be pre-specified. Hence the antenna gain , sidelobe levels can not be synthesized. Although Silver [3] has proposed the method of shaping the reflector surfaces by specifying the aperture illumination since 1949. This problem has been unsolved until the computer power was available in 1970's. Generally, the problem can be tackled in two ways:
(a) The feed radiation pattern and the main reflector aperture illumination are given. The profiles of main and subreflectors are to be optimized. This scenario is commonly encountered in the design of a new antenna.
(b) The feed radiation pattern and the main reflector profile are given. The subreflector profile is to be found by using phase uniform aperture illuminations. This is the most useful approach for upgrading those existing antenna systems designed by using the closed form solutions.

Pioneering works as to (a) and (b) have been carried out by Galindo [12] and

Potter [33], etc. In this chapter, Galindo's method of calculating the shaped reflector surfaces is presented and the results are used to design Cassegrain and Gregorian antennas for the large earth stations.

3.1 Axisymmetric Dual Reflector Antennas

For the dual reflector antenna, the main reflector is formed by rotating a parabola about its own axis and the subreflector is made similarly by rotating either an ellipse or hyperbola. The subreflector has two focal points. One focal point is also the phase center of the feed, and the second focal point is made to coincide with the focal point of the paraboloidal main reflector.

As shown in Figure 3.1, the Cassegrain antenna has a hyperboloidal subreflector. Hence, the second focal point is a virtual one. The Gregorian antenna, on the other hand, has a ellipsoidal subreflector with a real focal point, as shown in Figure 3.2.

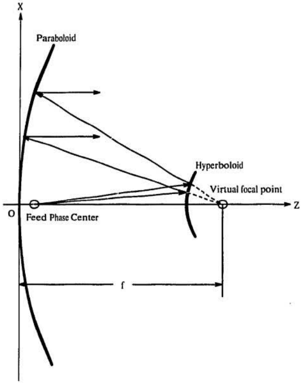

Figure 3.1: Cassegrain antenna configuration.

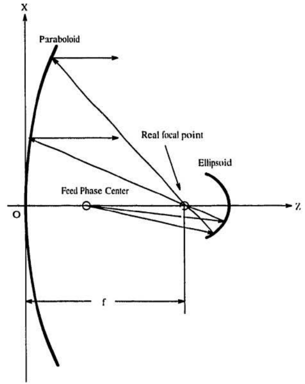

Figure 3.2: Gregorian antenna configuration.

3.2 Geometrical Optics (GO) Principles

In the ballistic theory of light, the propagation of electromagnetic energy is explained in terms of the kinematics of photo particles. Whether or not this hypothesis is nearer to physical reality than that of wave propagation, it does lead to a particularly useful concept, i.e. an optical ray as the trajectory of a photonics particle. The tangent to a ray at any point represents equally the local direction of propagation, or the normal to the wavefront. Also associated with the ray at any point is its intensity. Proportional to the latter are the ray field vector E and H in magnitude. Geometrical optics has a theoretical foundation based on Maxwell's equations and results from an asymptotic solution to these equations as the frequency ω tends to infinity [55].

In the non-closed form antenna designs, as long as the dimensions of the reflectors are very large compared with the wavelength, the method is successful. The basic principles of GO are:

(1) Snell's Law: At a point on the reflector surface, the incident and reflected rays as well as the surface normal vector are coplanar, then the angle of incidence equals to the angle of reflection.

(2) Conservation of energy law: Energy along each different tube of ray remains constant, even when the tube undergoes reflection.

(3) Malus law: The surfaces of the constant phase are normal to 'he ray trajectories even after a number of reflections. The ray length between two equal-phase surfaces keeps constant.

3.3 Cassegrain Antenna

3.3.1 Design Techniques

(i) Design of both main reflector and subreflector given the main reflector aperture illumination and the feed radiation pattern

The main reflector and subreflector of the Cassegrain antenna with revolutionally symmetric structure are shown in Figure 3.3. The profile of main reflector is described in rectangular coordinate (x, z) and that of subreflector is described in both rectangular coordinate (x', z') and polar coordinates (ρ, θ). The origin point of (x', z') is the feed phase center F. α is the distance between the two rectangular coordinate systems. The relationship among the three systems are:

$$\begin{aligned} x' &= x \\ x' &= \rho \sin\theta \\ z' &= \rho\cos\theta \\ z' - z &= \alpha \end{aligned}$$

If the subreflector surface is expressed as:

$$\rho = f(\theta)$$

or

$$S(\theta) = \rho - f(\theta) = 0,$$

then the unit vector normal to the subreflector surface is

$$\begin{aligned} \hat{n}_s &= \nabla S(\theta)/|\nabla S(\theta)| \\ &= \hat{x}[\frac{1}{\Delta}(-\frac{df}{d\theta}\cos\theta + f\sin\theta)] + \hat{z}[\frac{1}{\Delta}(\frac{df}{d\theta}\sin\theta + f\cos\theta)] \end{aligned}$$

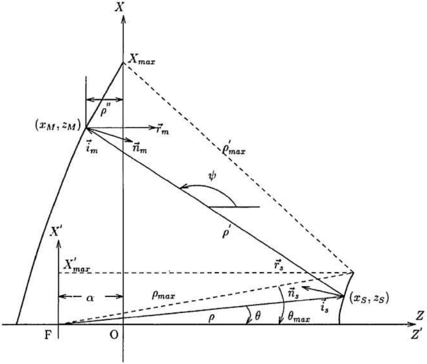

Figure 3.3: Geometrical optics for Cassegrain antenna reflectors shaping.

where

$$\Delta = [(\frac{df}{d\theta})^2 + f^2]^{\frac{1}{2}}$$

The incident vector is:

$$\hat{i}_s = \hat{\rho} = \hat{x}\sin\theta + \hat{z}\cos\theta$$

and the reflection vector is:

$$\hat{r}_s = \hat{x}\sin\psi + \hat{z}\cos\psi$$

From Snell's law, i.e., $\hat{n} \cdot \hat{r} = -\hat{i} \cdot \hat{n}$, the following expression can be obtained:

$$\frac{df}{d\theta} = \frac{d\rho}{d\theta} = \rho\cot(\frac{\psi - \theta}{2}) \qquad (3.1)$$

If the profile of main reflector surface is expressed as:

$$z = g(x)$$

or

$$M(x) = z - g(x) = 0$$

The unit vector normal to the main reflector surface is:

$$\hat{n} = -\frac{\nabla M(x)}{|\nabla M(x)|} = \frac{1}{D}[\frac{dg}{dx}\hat{x} - \hat{z}]$$

where

$$D = [(\frac{dg}{dx})^2 + 1]^{\frac{1}{2}}$$

The incident vector is:

$$\hat{i} = \hat{x}\sin\psi + \hat{z}\cos\psi$$

and the reflection vector is:

$$\hat{r} = \hat{z}$$

From Snell's law, the differential equation about the main reflector can be described as:

$$\frac{dz}{dx} = \cot(\frac{\psi}{2}) \tag{3.2}$$

If the feed pattern is known, the total radiated power within the increment $d\theta$ of the pattern $F(\theta)$ will be

$$F(\theta)2\pi\sin\theta d\theta$$

The total radiated power from $\theta = 0$ to angle θ_{max} will then be

$$2\pi\int_0^{\theta_{max}} F(\theta)\sin\theta d\theta$$

Similarly, if the desired illumination $I(x)$ is known, the power within the increment dx of the main reflector aperture is

$$I(x)2\pi x dx$$

Again, the total power within the region $(0, X_{max})$ is

$$\int_0^{X_{max}} I(x)2\pi x dx$$

From the conservation of energy law, the following equation can be derived:

$$\frac{dx}{d\theta} = A\frac{F(\theta)\sin\theta}{I(x)x} \tag{3.3}$$

where

$$A = \frac{\int_0^{X_{max}} I(x)x dx}{\int_0^{\theta_{max}} F(\theta)\sin\theta d\theta}$$

So the three differential equations, i.e., eq.(3.1), eq.(3.2) and eq.(3.3) are obtained with three unknowns, ρ, z and x. They are sufficient to determine the reflector profiles with the initial values of $\rho_{max}, \theta_{max}, X_{max}$. The *Runge-Kutta method* is employed to solve these differential equations. This approach is commonly used to design a new antenna.

(ii) Design of the only subreflector when the main reflector profile and feed radiation pattern are given

There exist a number of existing earth stations which do not meet the CCITT specification, especially the close-in and the far-angle sidelobe levels. The antenna need to be modified to upgrade its performances at the least cost. The redesign of the feed or/and the main reflector is normally more costly than the modification of the subreflector only. It is worthwhile to present the numerical approach for this particular design. The feed pattern is commonly assumed to be revolutionally symmetric and can be represented as $F(\theta)$. This assumption is often valid based on the fact that the subtented angle of the subreflector is usually small. The main reflector profile is given and can be expressed as

$$z = g(x)$$

Assume the power illumination on the main reflector aperture, $I(x)$, is phase uniform, this implies that the path length from the feed phase center to the aperture must be constant based on Malus law, using the same coordinate system shown in Figure 3.3, one has

$$\rho + \rho' + \rho'' = C$$

The constant length C can be obtained from the condition at the edges

$$C = \rho_{max} + \rho'_{max} \quad (\text{when } \rho'' = 0)$$

According to Figure 3.3,

$$\rho'' = -z_M$$

$$\rho' = \frac{x_M - x_S}{\sin\psi}$$

$$\rho = \sqrt{[x_S^2 + z_S^2]}$$

$$z_S = \alpha + \frac{x_S - x_M}{\tan\psi} + z_M \tag{3.4}$$

The following expression holds

$$[C + z_M - \frac{x_M - x_S}{\sin\psi}]^2 = x_S^2 + [\alpha + z_M + \frac{x_S - x_M}{\tan\psi}]^2$$

Then the x_S can be derived.

$$x_S = \frac{x_M^2 + 2x_M(\frac{z_M+\alpha}{\tan\psi} - \frac{C+z_M}{\sin\psi}) + (C-\alpha)(C+\alpha+2z_M)}{2(x_M + \frac{\alpha+z_M}{\tan\psi} - \frac{C+z_M}{\sin\psi})} \tag{3.5}$$

Because the main reflector profile is given, apply Snell's law on the main reflector, it is easily to obtain the following expression from eq.(3.2)

$$\psi = 2\arctan(\frac{dx}{dz})$$

The subreflector profile can be uniquely defined by eq.(3.4) and eq.(3.5).

3.3.2 Numerical Results

Based on above equations, the Cassegrain antenna reflectors design program is developed. The non-closed form solutions are obtained by using computer analyses. These shaped reflectors are the quasi-hyperboloidal subreflector and quasi-paraboloidal main reflector. Technique (i) is mostly employed and will be used later in this thesis. Technique (ii) is used only in the subreflector modification whenever an existing antenna is required to upgrade its performance.

(a) Design examples using technique (i)

Example 1:

Assume the feed radiation pattern is given and shown in Figure 3.4 which is obtained by using the corrugated conical horn analysis program (*Chapter 2*). The main reflector radius is 98.5″ and the subreflector radius is 14.0″. The feed phase center is located at $\alpha = -27.0''$ (Refer to Figure 3.3). The subreflector subtended angle related to the feed radiation pattern is 12.7°. This means that the feed radiation pattern is approximately taped $18dB$ down at the subreflector edge. Then the initial values are:

$$
\begin{aligned}
X_{max} &= 98.5'' \\
\theta_{max} &= 12.7^{\circ} \\
\rho_{max} &= \frac{X'_{max}}{\sin(\theta_{max})} = \frac{14.0''}{\sin(12.7^{\circ})}
\end{aligned}
$$

Taking the subreflector blockage and main reflector edge effect into consideration, the main reflector aperture illumination is assumed as shown in Figure 3.5. The calculated main and subreflector profiles are plotted in Figure 3.5. The surfaces are no longer the closed form paraboloidal and hyperboloidal reflectors but they are modified and become quasi-paraboloidal and quasi-hyperboloidal ones.

Example 2:

Assume the feed radiation pattern is given and shown in Figure 3.4 which is same as that in Example 1. The main reflector radius is 157.0″ and the subreflector radius is 24.0″. The feed phase center is located at $\alpha = -27.0''$ (Refer to Figure 3.3). The subreflector subtended angle related to the feed radiation pattern is also 12.7°. Then the initial values are:

$$\begin{aligned} X_{max} &= 157.0'' \\ \theta_{max} &= 12.7^o \\ \rho_{max} &= \frac{X'_{max}}{\sin(\theta_{max})} = \frac{24.0''}{\sin(12.7^o)} \end{aligned}$$

Taking the subreflector blockage and main reflector edge effect into consideration, the main reflector aperture illumination is assumed and shown in Figure 3.6. The calculated main and subreflector profiles are plotted in Figure 3.6. The surfaces are no longer paraboloidal and hyperboloidal reflectors but they are modified and become quasi-paraboloidal and quasi-hyperboloidal reflectors.

(b) Design example using technique (ii)

If the feed radiation pattern and the main reflector surface are given, using technique (ii), the surface profile of the subreflector can be obtained. A specific subreflector reshaping program is developed. As an example, taking the main reflector profile found in Example 1 as a known one and using technique (ii), the subreflector profile can be calculated and shown in Figure 3.7.

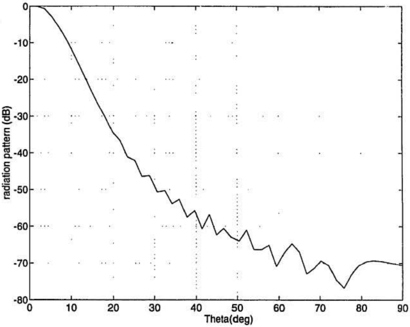

Figure 3.4: Radiation pattern of the corrugated conical horn. Frequency: 14.25GHz, Aperture radius: 8.0*in*, Flare angle: 12°

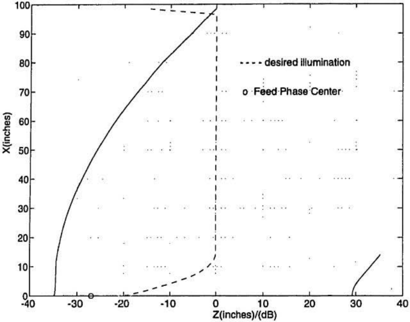

Figure 3.5: Shaped Cassegrain main and subreflector profiles (Example 1). Solid line: reflector profiles (Unit: inches), Dotted line: main reflector aperture illumination (Unit: dB)

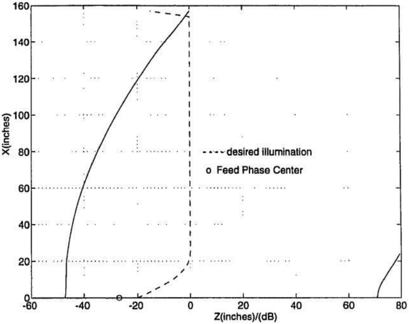

Figure 3.6: Shaped Cassegrain main and subreflector profiles (Example 2). Solid line: reflector profiles (Unit: inches), Dotted line: main reflector aperture illumination (Unit: dB)

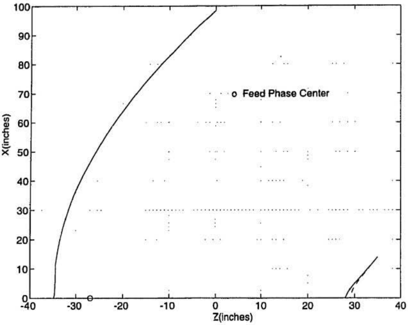

Figure 3.7: Reshaped Cassegrain subreflector profile (Unit: inches). Solid line: subreflector profile after reshaping, Dotted line: subreflector profiles before reshaping

3.4 Gregorian Antenna

3.4.1 Design Techniques

The main and subreflectors of the Gregorian antenna with revolutionally symmetric structure are shown in Figure 3.8. The profile of main reflector is described in rectangular coordinate (x, z) and that of subreflector is described in both rectangular coordinate (x', z') and polar coordinates (ρ, θ). The origin point of (x', z') is the feed phase center F. α is the distance between the two rectangular coordinate systems. The relationships between these three systems are:

$$
\begin{aligned}
x' &= x \\
x' &= \rho \sin\theta \\
z' &= \rho \cos\theta \\
z' - z &= \alpha
\end{aligned}
$$

If the subreflector surface is expressed as:

$$\rho = f(\theta)$$

or

$$S(\theta) = \rho - f(\theta) = 0,$$

then the unit vector normal to the subreflector surface is

$$
\begin{aligned}
\hat{n} &= -\nabla S(\theta)/|\nabla S(\theta)| \\
&= -\hat{x}[\frac{1}{\Delta}(-\frac{df}{d\theta}\cos\theta + f\sin\theta)] - \hat{z}[\frac{1}{\Delta}(\frac{df}{d\theta}\sin\theta + f\cos\theta)]
\end{aligned}
$$

where

$$\Delta = [(\frac{df}{d\theta})^2 + f^2]^{\frac{1}{2}}$$

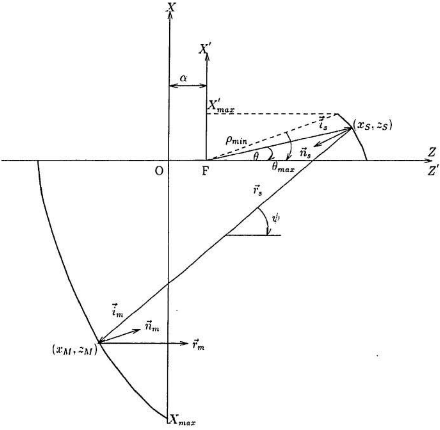

Figure 3.8: Geometrical optics for Gregorian antenna reflectors shaping.

The incident vector is:

$$\hat{i} = \hat{\rho} = \hat{x} \sin\theta + \hat{z} \cos\theta$$

and the reflection vector is expressed using ψ:

$$\hat{r} = -\hat{x} \sin\psi - \hat{z} \cos\psi$$

From Snell's law, i.e., $\hat{n} \cdot \hat{r} = -\hat{i} \cdot \hat{n}$, the following expression can be obtained:

$$\frac{df}{d\theta} = \frac{d\rho}{d\theta} = \rho \cot\left(\frac{\psi - \theta}{2}\right) \tag{3.6}$$

If the profile of main reflector surface is expressed as:

$$z = g(x)$$

or

$$M(x) = z - g(x) = 0$$

The unit vector normal to the main reflector surface is:

$$\hat{n}_m = -\frac{\nabla M(x)}{|\nabla M(x)|} = \frac{1}{D}[\frac{dg}{dx}\hat{x} - \hat{z}]$$

where

$$D = [(\frac{dg}{dx})^2 + 1]^{\frac{1}{2}}$$

The incident vector is:

$$\hat{i}_m = -\hat{x} \sin\psi - \hat{z} \cos\psi$$

and the reflection vector is:

$$\hat{r}_m = \hat{z}$$

From Snell's law, the differential equation about the main reflector can be described as:

$$\frac{dz}{dx} = -\tan(\frac{\psi}{2}) \tag{3.7}$$

If the feed radiation pattern is known, the total radiated power within the increment $d\theta$ of the pattern $F(\theta)$ will be

$$F(\theta) 2\pi \sin\theta d\theta$$

The total radiated power from $\theta = 0$ to angle θ_{max} will then be

$$2\pi \int_0^{\theta_{max}} F(\theta) \sin\theta d\theta$$

Similarly, if the desired illumination $I(x)$ is known, the power within the increment dx of the main reflector aperture is

$$I(x) 2\pi x dx$$

Again, the total power within the region $(0, X_{max})$ is

$$\int_0^{X_{max}} I(x) 2\pi x dx$$

From the conservation of energy law, the following equation can be derived:

$$\frac{dx}{d\theta} = A \frac{F(\theta) \sin\theta}{I(x) x} \tag{3.8}$$

where

$$A = \frac{\int_0^{X_{max}} I(x) x dx}{\int_0^{\theta_{max}} F(\theta) \sin\theta d\theta}$$

So the three differential equations, i.e., eq.(3.6), eq.(3.7) and eq.(3.8) are obtained with three unknowns ρ, z, and x. They are sufficient to determine the reflector profiles with the initial values of $\rho_{min}, \theta_{max}, X_{max}$. The *Runge-Kutta method* is employed to solve these differential equations.

3.4.2 Numerical Results

Based on above technique, the Gregorian antenna reflectors design program is developed. Both the main and the subreflector can be designed if the feed radiation pattern is known and the main aperture illumination is specified.

Example 3:

In this example. the feed radiation pattern is the same as shown in Figure 3.4 and the desired main aperture illumination is shown in Figure 3.9. The feed phase center is located at $\alpha = 27.0''$ (Refer to Figure 3.8). The radius of main reflector is $98.5''$ and the radius of subreflector is $14.0''$. The subtented angle of subreflector related to the feed radiation pattern is 12.7^o. This means that the feed radiation pattern is approximately $18dB$ down at the subreflector edge. Then the initial values are:

$$\begin{aligned} X_{max} &= 98.5'' \\ \theta_{max} &= 12.7^o \\ \rho_{min} &= \frac{X'_{max}}{\sin(\theta_{max})} = \frac{14.0''}{\sin(12.7^o)} \end{aligned}$$

The calculated main reflector profile and subreflector profile are plotted in Figure 3.9. The surfaces are no longer the closed form paraboloidal and ellipsoidal reflectors but they are modified to become quasi-paraboloidal and quasi-ellipsoidal ones.

Example 4:

Assume the feed radiation pattern is given and shown in Figure 3.4 which is the same as that in Example 3. The main reflector radius is 157.0" and the subreflector radius is 24.0". The feed phase center is located at $\alpha = 27.0''$ (Refer to Figure 3.8). The subreflector subtended angle related to the feed radiation pattern is also 12.7°. Then the initial values are:

$$\begin{aligned} X_{max} &= 157.0'' \\ \theta_{max} &= 12.7^{o} \\ \rho_{max} &= \frac{X'_{max}}{\sin(\theta_{max})} = \frac{24.0''}{\sin(12.7^{o})} \end{aligned}$$

Taking the subreflector blockage and main reflector edge effect into consideration, the main reflector aperture illumination is assumed and shown in Figure 3.10. The calculated main and subreflector profiles are plotted in Figure 3.10. The surfaces are no longer paraboloidal and ellipsoidal reflectors but they are modified to become quasi-paraboloidal and quasi-ellipsoidal reflectors.

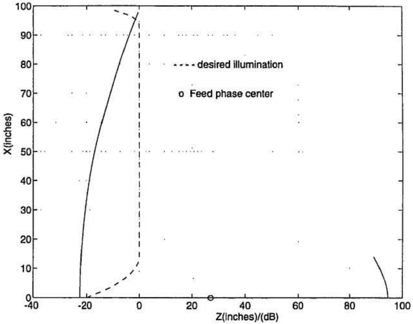

Figure 3.9: Shaped Gregorian main and subreflector profiles (Example 3). Solid line: reflector profiles (Unit: inches), Dotted line: main reflector aperture illumination (Unit: dB)

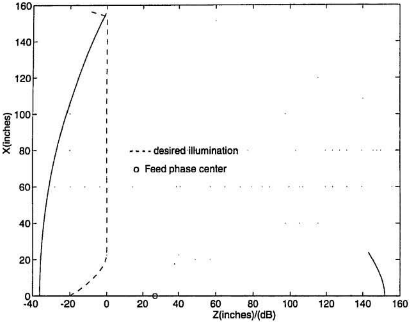

Figure 3.10: Shaped Gregorian main and subreflector profiles (Example 4). Solid line: reflector profiles (Unit: inches). Dotted line: main reflector aperture illumination (Unit: dB)

Chapter 4

Dual Shaped Reflector Antenna Analysis

The objective of this chapter is to provide various detailed performances of the dual reflector antenna. The corrugated conical horn described in *Chapter 2* is used as the only antenna feed. The circularly symmetrical reflector profiles generated in *Chapter 3* are employed for investigating the scattered patterns of the subreflectors and the radiation patterns of the main reflectors with the physical optics (PO) technique. Having knowledge the radiation patterns, the antenna performances such as boresight gain , sidelobe levels, spillovers and etc., can be obtained. Thus, the antenna characteristics as well as its performance trade-offs can be fully carried out.

4.1 Theory of Physical Optics (PO)

The radiation fields of any given reflector can be obtained by integrating directly over the induced surface currents which are physically responsible for initiating the radiation. Alternatively, they can be calculated from the fields incident on the reflector. Although there are various applicable integrals, all of them arise essentially from the application of Green's vector identities to Maxwell's equations. In this thesis, the vector Kirchhoff diffraction integrals will be employed.

In free space, the fields scattered by a induced surface current can be approximated as [3]:

$$
\begin{aligned}
\vec{E}_p &= -\frac{j}{4\pi\omega\epsilon_0}\int\int_s[(\vec{J}\cdot\nabla)\nabla + k^2\vec{J} - j\omega\epsilon_0\vec{J}_m \times \nabla]\frac{e^{-jkr}}{r}dS \\
\vec{H}_p &= -\frac{j}{4\pi\omega\mu_0}\int\int_s[(\vec{J}_m\cdot\nabla)\nabla + k^2\vec{J}_m + j\omega\mu_0\vec{J}\times\nabla]\frac{e^{-jkr}}{r}dS
\end{aligned}
$$

where $\vec{J}$ and $\vec{J}_m$ are the electric and magnetic current distributions on the surface. $k = \omega\sqrt{\mu_0\epsilon_0}$. ∇ takes effect on S only, i.e., ∇ acts on the coordinates of source element.

If the reflector surface is perfect conductor, then $\vec{J}_m = 0$. The scattered fields can be written as:

$$
\begin{aligned}
\vec{E}_p &= -\frac{j}{4\pi\omega\epsilon_0}\int\int_s[(\vec{J}\cdot\nabla)\nabla + k^2\vec{J}]\frac{e^{-jkr}}{r}dS \\
\vec{H}_p &= \frac{1}{4\pi}\int\int_s(\vec{J}\times\nabla)\frac{e^{-jkr}}{r}dS
\end{aligned}
$$

As shown in Figure 4.1, $\vec{\rho}$ is the vector from the origin to the source element point, $\vec{R}$ is the vector from origin to the far field point P. $\vec{r}$ is the vector from source element to the far field point P, and $\hat{\rho}$, $\hat{R}$ and $\hat{r}$ are unit vectors, respectively. The following identities hold.

$$
\begin{aligned}
\nabla(\frac{e^{-jkr}}{r}) &= (jk+\frac{1}{r})\frac{e^{-jkr}}{r}\hat{r} \\
(\vec{J}\cdot\nabla)\nabla\frac{e^{-jkr}}{r} &= [-k^2(\vec{J}\cdot\hat{r})\hat{r} + \frac{3}{r}(jk+\frac{1}{r})(\vec{J}\cdot\hat{r})\hat{r} - \vec{J}\frac{1}{r}(jk+\frac{1}{r})]\frac{e^{-jkr}}{r} \\
(\vec{J}\times\nabla)\frac{e^{-jkr}}{r} &= (jk+\frac{1}{r})\frac{e^{-jkr}}{r}(\vec{J}\times\hat{r})
\end{aligned}
$$

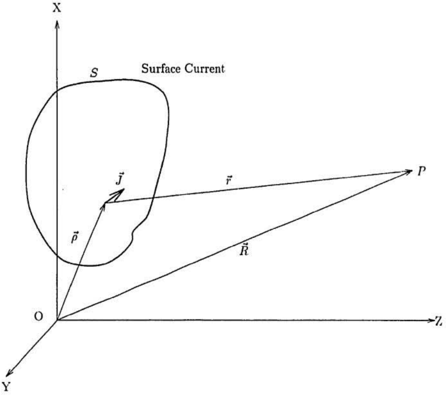

Figure 4.1: Co-ordinate system used for evaluating the vector Kirchhoff diffraction integration.

For the far fields, the observation point P is very far from the current sources, $\vec{r}$ and $\vec{R}$ are almost parallel, then $\vec{r}$ in the phase term such as $e^{-jk\vec{r}}$ where r should be approximated as:

$$r \approx R - \vec{\rho} \cdot \hat{R}$$

and in the magnitude term, one should have:

$$|\vec{r}| \approx |\vec{R}|$$

Using the above identities and neglecting the $1/r^2$ and $1/r^3$ terms, the far fields can be approximated as:

$$\vec{E}_p = -\frac{j\omega\mu_0}{4\pi R} e^{-jkR} \int\int_s [\vec{J} - (\vec{J} \cdot \hat{r})\hat{r}] e^{jk\vec{\rho}\cdot\hat{R}} dS \tag{4.1}$$

$$\vec{H}_p = -\frac{j\omega\epsilon_0}{4\pi R} e^{-jkR} \int\int_s [-(\frac{\mu_0}{\epsilon_0})^{\frac{1}{2}} \vec{J} \times \hat{r}] e^{jk\vec{\rho}\cdot\hat{R}} dS \tag{4.2}$$

From eq.(4.1) and eq.(4.2), it can be observed that in the far field zone

$$\begin{aligned} & \hat{R} \times \vec{H}_p - (\frac{\epsilon_0}{\mu_0})^{\frac{1}{2}} \vec{E}_p \\ \approx & \ \hat{r} \times \vec{H}_p - (\frac{\epsilon_0}{\mu_0})^{\frac{1}{2}} \vec{E}_p \\ = & \ \frac{e^{-jkR}}{4\pi R} \int\int_s \{j\omega(\mu_0\epsilon_0)^{\frac{1}{2}} [\hat{r} \times (\vec{J} \times \hat{r}) - \vec{J} + (\vec{J} \cdot \hat{r})\hat{r}]\} e^{jk\vec{\rho}\cdot\hat{R}} dS \\ = & \ 0 \end{aligned}$$

in which the following identity is used:

$$\hat{r} \times (\vec{J} \times \hat{r}) = (\hat{r} \cdot \hat{r})\vec{J} - (\hat{r} \cdot \vec{J})\hat{r} = \vec{J} - (\vec{J} \cdot \hat{r})\hat{r}$$

It is obvious that the scattered waves become plane wave in the far field zone, then $\vec{E}_p$, $\vec{H}_p$ and $\vec{R}$ are mutually perpendicular to each other.

The induced surface current due to the incident wave can be expressed as:

$$\vec{J}_s = 2\hat{n}_s \times \vec{H}_i \tag{4.3}$$

where $\hat{n}_s$ is the unit normal vector, $\vec{H}_i$ is the incident magnetic field and $\vec{J}_s$ is the induced surface electric current.

The physical optics (PO) will be used to evaluate the scattered patterns of the subreflector and the radiation patterns of the main reflector in the following sections.

4.2 Subreflector Scattered Patterns

In order to derive the radiation patterns of the main reflector, the scattered pattern of the subreflector must be calculated to provide the incident fields at the main reflector.

4.2.1 Coordinate System Definition

The coordinate systems used to analyze the scattered patterns of the subreflector are shown in Figure 4.2. Three coordinate systems are required in the following calculation:

(1). (X_f, Y_f, Z_f) and $(\rho_f, \theta_f, \phi_f)$:

the rectangular and spherical coordinate systems for the feed.

(2). (X_s, Y_s, Z_s) and $(\rho_s, \theta_s, \phi_s)$:

the rectangular and spherical coordinate systems for the subreflector.

(3). (X_m, Y_m, Z_m) and $(\rho_m, \theta_m, \phi_m)$:

the rectangular and spherical coordinate systems for the main reflector.

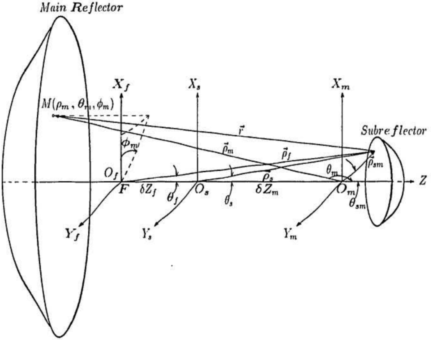

Figure 4.2: Co-ordinate system used in the analysis of the scattered patterns of the subreflector.

The Z axis is used as the rotationally symmetric axis for both Cassgrain and Grogorian types. Then the profile of the subreflector is generally defined by

$$\rho_s = f(\theta_s)$$

The surface profiles can be obtained by the design procedure described in *Chapter 3.*

The observation point $M(\rho_m, \theta_m, \phi_m)$ is assumed to be on the surface of the main reflector.

4.2.2 Feed Radiation Pattern

The corrugated conical horn is used as the earth station dual shaped reflector antenna feed. F or O_f is the feed phase center. Z axis is the revolutional axis of the horn. The feed radiated fields can be expressed in different forms according to the specified polarization.

In general, the E and H fields can be written as:

$$\begin{aligned} \vec{E}_f &= [E_{\theta_f}(\theta_f, \phi_f)\hat{\theta}_f + E_{\phi_f}(\theta_f, \phi_f)\hat{\phi}_f]\frac{e^{-jk\rho_f}}{\rho_f} && (4.4) \\ \vec{H}_f &= (\frac{\epsilon_0}{\mu_0})^{\frac{1}{2}}\hat{\rho}_f \times \vec{E}_f \\ &= (\frac{\epsilon_0}{\mu_0})^{\frac{1}{2}}[E_{\theta_f}(\theta_f, \phi_f)\hat{\phi}_f - E_{\phi_f}(\theta_f, \phi_f)\hat{\theta}_f]\frac{e^{-jk\rho_f}}{\rho_f} && (4.5) \end{aligned}$$

For vertical or X-polarization, the E field can be expressed as:

$$\vec{E}_f = [g_{\theta_f}(\theta_f)\cos\phi_f\hat{\theta}_f - g_{\phi_f}(\theta_f)\sin\phi_f\hat{\phi}_f]\frac{e^{-jk\rho_f}}{\rho_f}$$

For horizontal Y-polarization, the E field can be expressed as:

$$\vec{E}_f = [g_{\theta_f}(\theta_f)\sin\phi_f\hat{\theta}_f + g_{\phi_f}(\theta_f)\cos\phi_f\hat{\phi}_f]\frac{e^{-jk\rho_f}}{\rho_f}$$

In order to make use of the physical optics, the feed radiation patterns need to be expressed in the coordinate system $(\rho_s, \theta_s, \phi_s)$. Based on Figure 4.2, the following transformation relationships between the two coordinate systems $(\rho_f, \theta_f, \phi_f)$ and $(\rho_s, \theta_s, \phi_s)$ can be found:

$$
\begin{aligned}
\hat{\phi}_f &= \hat{\phi}_s \\
\phi_f &= \phi_s \\
\rho_s \sin\theta_s &= \rho_f \sin\theta_f \\
\rho_f \cos\theta_f &= \delta Z_f + \rho_s \cos\theta_s \\
\rho_f &= \sqrt{\rho_s^2 + (\delta Z_f)^2 + 2\rho_s \delta Z_f \cos\theta_s} && (4.6) \\
\theta_f &= \arccos(\frac{\delta Z_f + \rho_s \cos\theta_s}{\rho_f}) && (4.7) \\
\hat{\theta}_f &= \cos(\theta_s - \theta_f)\hat{\theta}_s + \sin(\theta_s - \theta_f)\hat{\rho}_s && (4.8)
\end{aligned}
$$

Eq.(4.8) is proved in *Appendix A*.

Using above relations, the magnetic field given in eq.(4.5) can be expressed according to the coordinates $(\rho_s, \theta_s, \phi_s)$:

$$\vec{H}_f = (\frac{\epsilon_0}{\mu_0})^{\frac{1}{2}}\{E_{\theta_f}(\theta_s, \phi_s)\varphi_s - E_{\phi_f}(\theta_s, \phi_s)[\cos(\theta_s - \theta_f)\hat{\theta}_s + \sin(\theta_s - \theta_f)\hat{\rho}_s]\}\frac{e^{-jk\rho_f}}{\rho_f} \quad (4.9)$$

where θ_f and ρ_f can be substituted by eq.(4.6) and eq.(4.7). Here we still use ρ_f and θ_f for simplicity.

4.2.3 Current Distribution On the Subreflector Surface

The current on the subreflector surface can be calculated using eq.(4.3). For a given surface of $\rho = f(\theta, \phi)$, its normal unit vector is given by

$$\hat{n} = \quad \hat{x}_s(f_\phi \sin\phi - f_\theta \sin\theta\cos\theta\cos\phi + f\sin^2\theta\cos\phi)/\Delta$$

$$+ \quad \hat{y}_s(-f_\phi \cos\phi - f_\theta \sin\theta \cos\theta \sin\phi + f \sin^2\theta \sin\phi)/\Delta$$

$$+ \quad \hat{z}_s(f \sin\theta \cos\theta + f_\theta \sin^2\theta)/\Delta$$

where

$$\Delta = (f_\phi^2 + f_\theta^2 \sin_\theta^2 + f^2 \sin_\theta^2)^{\frac{1}{2}}$$

$$f_\theta = \frac{\partial f}{\partial \theta}, \quad f_\phi = \frac{\partial f}{\partial \phi}$$

Due to the rotationally symmetric about the Z axis, $f_\phi = 0$, then

$$\begin{aligned} \hat{n} = & \quad \hat{x}_s(-f_\theta \sin\theta \cos\theta \cos\phi + f \sin^2\theta \cos\phi)/\Delta \\ & + \hat{y}_s(-f_\theta \sin\theta \cos\theta \sin\phi + f \sin^2\theta \sin\phi)/\Delta \\ & + \hat{z}_s(f \sin\theta \cos\theta + f_\theta \sin^2\theta)/\Delta \end{aligned}$$

where

$$\Delta = (f_\theta^2 + f^2)^{\frac{1}{2}} \sin\theta$$

or

$$\begin{aligned} \hat{n} = & \quad -\hat{x}_s(f_\theta \cos\theta - f \sin\theta) \cos\phi/\Delta' \\ & - \hat{y}_s(f_\theta \cos\theta - f \sin\theta) \sin\phi/\Delta' \\ & + \hat{z}_s(f \cos\theta + f_\theta \sin\theta)/\Delta' \end{aligned}$$

where

$$\Delta' = (f_\theta^2 + f^2)^{\frac{1}{2}}$$

Since the Cassegrain antenna uses the hyperboloidal subreflector, $\hat{n}_s$ must be an outward normal unit vector, then $\hat{n}_s = \hat{n}$.

In Gregorian antenna configuration, the subreflector is an ellipsoid. $\hat{n}_s$ is the inward normal unit vector, then $\hat{n}_s = -\hat{n}$. In the following derivation, the Gregorian antenna subreflector is used.

By using the following transformation relationships:

$$\begin{aligned}
\hat{x}_s &= \hat{\rho}_s \sin\theta_s \cos\phi_s + \hat{\theta}_s \cos\theta_s \cos\phi_s - \hat{\phi}_s \sin\phi_s \\
\hat{y}_s &= \hat{\rho}_s \sin\theta_s \sin\phi_s + \hat{\theta}_s \cos\theta_s \sin\phi_s + \hat{\phi}_s \cos\phi_s \\
\hat{z}_s &= \hat{\rho}_s \cos\theta_s - \hat{\theta}_s \sin\theta_s
\end{aligned}$$

the inward normal unit vector to the ellipsoidal subreflector can be proved to be given as:

$$\hat{n_s} = -f\hat{\rho}_s/\Delta' + f_\theta\hat{\theta}_s/\Delta' \tag{4.10}$$

Substituting eq.(4.9) and eq.(4.10) into eq.(4.3), neglecting the current distribution on the back surface of the subreflector, we have

$$\begin{aligned}
\vec{J}_s &= 2\hat{n}_s \times \vec{H}_i \\
&= 2(-\frac{f}{\Delta'}\hat{\rho}_s + \frac{f_\theta}{\Delta'}\hat{\theta}_s) \times [E_{\theta_f}(\theta_s, \phi_s)\hat{\phi}_s - E_{\phi_f}(\theta_s, \phi_s)\cos(\theta_s - \theta_f)\hat{\theta}_s \\
&\quad -E_{\phi_f}(\theta_s, \phi_s)\sin(\theta_s - \theta_f)\hat{\rho}_s](\frac{\epsilon_0}{\mu_0})^{\frac{1}{2}}\frac{e^{-jk\rho_f}}{\rho_f} \\
&= 2(\frac{\epsilon_0}{\mu_0})^{\frac{1}{2}}\frac{e^{-jk\rho_f}}{\rho_f}[\frac{f}{\Delta'}E_{\theta_f}\hat{\theta}_s + \frac{f}{\Delta'}E_{\phi_f}\cos(\theta_s - \theta_f)\hat{\phi}_s + \frac{f_\theta}{\Delta'}E_{\theta_f}\hat{\rho}_s \\
&\quad +\frac{f_\theta}{\Delta'}E_{\phi_f}\sin(\theta_s - \theta_f)\hat{\phi}_s]
\end{aligned} \tag{4.11}$$

4.2.4 Scattered Field Patterns

The far scattered H field due to the subreflector surface current can be evaluated by:

$$\vec{H}_s = \frac{1}{4\pi}jk \int\int_s (\vec{J}_s \times \hat{r})\frac{e^{-jkr}}{r}dS \tag{4.12}$$

Because the scattered fields from the subreflector are the incident fields to the main reflector, in order to derive the induced current on the main reflector which is responsible for the radiation patterns of the antenna, the scattered fields need to be expressed in the main reflector coordinate system.

In Figure 4.2, if O_m is close to subreflector and $M(\rho_m, \theta_m, \phi_m)$ is far away from subreflector, then

$$\begin{aligned} r &\approx \rho_m - \rho_s \sin\theta_s \sin\theta_m \cos(\phi_s - \phi_m) - \rho_s \cos\theta_s \cos\theta_m + \delta Z_m \cos\theta_m \\ \frac{e^{-jkr}}{r} &\approx \frac{1}{\rho_m}[e^{-jk\rho_m} \cdot e^{jk\rho_s \sin\theta_s \sin\theta_m \cos(\phi_s - \phi_m)} \cdot e^{jk\rho_s \cos\theta_s \cos\theta_m} \cdot e^{\delta Z_m \cos\theta_m}] \end{aligned}$$

Using the proof given in *Appendix B*, the differential subreflector surface element can be expressed as:

$$\begin{aligned} dS &= f[f_\phi^2 + f_\theta^2 \sin^2\theta_s + f^2 \sin^2\theta_s]^{\frac{1}{2}} d\theta_s d\phi_s \\ &= f(f_\theta^2 + f^2)^{\frac{1}{2}} \sin\theta_s d\theta_s d\phi_s \\ &= f\Delta' \sin\theta_s d\theta_s d\phi_s \end{aligned} \tag{4.13}$$

Then eq.(4.12) becomes

$$\begin{aligned} \vec{H}_s = {} & \frac{jk}{2\pi}(\frac{\epsilon_0}{\mu_0})^{\frac{1}{2}} \cdot \frac{e^{-jk\rho_m}}{\rho_m} \cdot e^{\delta Z_m \cos\theta_m} \\ & \int_{\theta s}\int_{\phi_s} e^{jk\rho_s \cos\theta_s \cos\theta_m} \cdot e^{-jk\rho_f}(\frac{f}{\rho_f}) \sin\theta_s \\ & \{[fE_{\theta_f}\hat{\theta}_s + fE_{\phi_f}\cos(\theta_s - \theta_f) + f_\theta E_{\theta_f}\hat{\rho}_s + f_\theta E_{\phi_f}\sin(\theta_s - \theta_f)\hat{\phi}_s] \\ & \times\hat{\rho_m} \cdot e^{jk\rho_s \sin\theta_s \sin\theta_m \cos(\phi_s - \phi_m)} d\phi_s\} d\theta_s \end{aligned} \tag{4.14}$$

Applying the identities given in *Appendix C*, the components of $\vec{H}_s$ can be written as:

$$\vec{H}_s \cdot \hat{\theta_m} = \frac{jk}{2\pi}(\frac{\epsilon_0}{\mu_0})^{\frac{1}{2}} \cdot \frac{e^{-jk\rho_m}}{\rho_m} \cdot e^{\delta Z_m \cos\theta_m} \int_{\theta s}\int_{\phi_s} e^{jk\rho_s \cos\theta_s \cos\theta_m} \cdot e^{-jk\rho_f}(\frac{f}{\rho_f}) \sin\theta_s$$

$$
\begin{aligned}
&\{fE_{\theta_f}\cos\theta_s\sin(\phi_s-\phi_m)\\
&+[fE_{\phi_f}\cos(\theta_s-\theta_f)+f_\theta E_{\phi_f}\sin(\theta_s-\theta_f)]\cos(\phi_s-\phi_m)\\
&+f_\theta E_{\theta_f}\sin\theta_s\sin(\phi_s-\phi_m)\}\cdot e^{jk\rho_s\sin\theta_s\sin\theta_m\cos(\phi_s-\phi_m)}d\phi_s d\theta_s
\end{aligned}
\tag{4.15}
$$

$$
\begin{aligned}
\vec{H}_s\cdot\hat{\phi_m} = {} & \frac{jk}{2\pi}(\frac{\epsilon_0}{\mu_0})^{\frac{1}{2}}\cdot\frac{e^{-jk\rho_m}}{\rho_m}\cdot e^{\delta Z_m\cos\theta_m}\int_{\theta_s}\int_{\phi_s}e^{jk\rho_s\cos\theta_s\cos\theta_m}\cdot e^{-jk\rho_f}(\frac{f}{\rho_f})\sin\theta_s\\
&\{-fE_{\cdot_f}[\cos\theta_m\cos\theta_s\cos(\phi_s-\phi_m)+\sin\theta_s\sin\theta_m]\\
&+[fE_{\phi_f}\cos(\theta_s-\theta_f)+f_\theta E_{\phi_f}\sin(\theta_s-\theta_f)]\cos\theta_m\sin(\phi_s-\phi_m)\\
&+f_\theta E_{\theta_f}[-\sin\theta_s\sin\theta_m\cos(\phi_s-\phi_m)+\cos\theta_s\sin\theta_m]\}\\
&\cdot e^{jk\rho_s\sin\theta_s\sin\theta_m\cos(\phi_s-\phi_m)}d\phi_s d\theta_s
\end{aligned}
$$

For the vertical or X-polarization, we have

$$
\begin{aligned}
E_{\theta_f} &= g_{\theta_f}(\theta_f)\cos\phi_f\\
E_{\phi_f} &= -g_{\phi_f}(\theta_f)\sin\phi_f
\end{aligned}
$$

Using the coordinate transformation, the above expressions can be written as:

$$
\begin{aligned}
E_{\theta_f} &= g_\theta(\theta_s)\cos\phi_s\\
E_{\phi_f} &= -g_\phi(\theta_s)\sin\phi_s
\end{aligned}
$$

Putting these equations into $\vec{H}_s$ and using the integration identities given in *Appendix D*, the scattered H field can be expressed as:

$$
\begin{aligned}
\vec{H}_s\cdot\hat{\theta_m} &= h_\theta(\theta_m)\sin\phi_m\cdot\frac{e^{-jk\rho_m}}{\rho_m}(\frac{\epsilon_0}{\mu_0})^{\frac{1}{2}}\\
&= \frac{jk}{2\pi}(\frac{\epsilon_0}{\mu_0})^{\frac{1}{2}}\cdot\frac{e^{-jk\rho_m}}{\rho_m}\cdot e^{\delta Z_m\cos\theta_m}\sin\phi_m\int_{\theta_s}e^{jk\rho_s\cos\theta_s\cos\theta_m}\cdot e^{-jk\rho_f}(\frac{f}{\rho_f})\sin\theta_s\\
&\quad\{-(fg_\theta\cos\theta_s+f_\theta g_\theta\sin\theta_s)[J_0(x_s)+J_2(x_s)]
\end{aligned}
$$

$$-[fg_\phi \cos(\theta_s-\theta_f)+f_\theta g_\phi \sin(\theta_s-\theta_f)]\cdot[J_0(x_s)-J_2(x_s)]\}d\theta_s \qquad (4.16)$$

$$\begin{aligned}
\vec{H}_s\cdot\hat{\phi_m} &= h_\phi(\theta_m)\cos\phi_m\cdot\frac{e^{-jk\rho_m}}{\rho_m}\left(\frac{\epsilon_0}{\mu_0}\right)^{\frac{1}{2}} \\
&= \frac{jk}{2}\left(\frac{\epsilon_0}{\mu_0}\right)^{\frac{1}{2}}\cdot\frac{e^{-jk\rho_m}}{\rho_m}\cdot e^{\delta Z_m\cos\theta_m}\sin\phi_m\int_{\theta_s} e^{jk\rho_s\cos\theta_s\cos\theta_m}\cdot e^{-jk\rho_f}\left(\frac{f}{\rho_f}\right)\sin\theta_s \\
&\quad \{-(fg_\theta\cos\theta_s\cos\theta_m+f_\theta g_\theta\sin\theta_s\sin\theta_m)[J_0(x_s)-J_2(x_s)] \\
&\quad -2j(fg_\theta\sin\theta_s\sin\theta_m-f_\theta g_\theta\cos\theta_s\sin\theta_m)J_1(x_s) \\
&\quad -[fg_\phi\cos(\theta_s-\theta_f)\cos\theta_m+f_\theta g_\phi\sin(\theta_s-\theta_f)\cos\theta_m] \\
&\quad \cdot[J_0(x_s)-J_2(xs)]\}d\theta_s \qquad (4.17)
\end{aligned}$$

where $x_s = k\rho_s\sin\theta_s\sin\theta_m$.

The E field can be obtained by

$$\vec{E}_s = -\left(\frac{\mu_0}{\epsilon_0}\right)^{\frac{1}{2}}\hat{\rho_m}\times\vec{H}_s$$

These are the incident fields on the main reflector.

4.3 Main Reflector Field Patterns

4.3.1 Coordinate System Definition

The coordinate system used to analyze the field patterns of the main reflector is shown in Figure 4.3. The rectangular and spherical coordinate systems for the main reflector are (X_m, Y_m, Z_m) and $(\rho_m, \theta_m, \phi_m)$. The far field observation point is $P(R_p, \theta_p, \phi_p)$.

Using the rotationally symmetry, the profile of the main reflector can generally be defined as:

$$\rho_m = F(\theta_m)$$

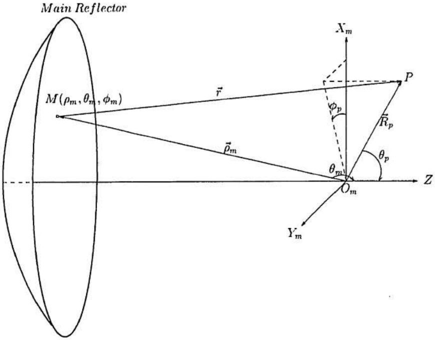

Figure 4.3: Co-ordinate system used in the analysis of the radiation pattern of the main reflector.

The surface profile can be obtained by using the design procedure described in *Chapter 3.*

4.3.2 Current Distribution on the Main Reflector

We can express the scattered pattern of the subreflector in a concise form :

$$\begin{aligned} \vec{H}_s &= [H_\theta(\theta_m, \phi_m)\hat{\theta_m} + H_\phi(\theta_m, \phi_m)\hat{\phi_m}]\frac{e^{-jk\rho_m}}{\rho_m}(\frac{\epsilon_0}{\mu_0})^{\frac{1}{2}} \\ &= [H_\theta\hat{\theta_m} + H_\phi\hat{\phi_m}]\frac{e^{-jk\rho_m}}{\rho_m}(\frac{\epsilon_0}{\mu_0})^{\frac{1}{2}} \end{aligned}$$

The $\vec{H}_s$ field can induce the electric current on the main reflector. The coordinate system for the radiation pattern calculation is shown in Figure 4.3. The induced current at the point $M(\rho_m, \theta_m, \phi_m)$ on the main reflector is given by:

$$\vec{J}_m = 2\hat{n}_m \times \vec{H}_s(M)$$

Assume the main reflector surface profile is

$$\rho_m = F(\theta_m)$$

Following the steps given in *Section 4.2.3*, the inward normal unit vector of the main reflector can be obtained by:

$$\begin{aligned} \hat{n}_m &= -\hat{\rho}_m \frac{F}{\Delta} + \hat{\theta}_m \frac{F_\theta}{\Delta} \\ dS &= F\Delta \sin\theta_m d\theta d\phi \end{aligned}$$

where

$$\Delta = (F_\theta^2 + F^2)^{\frac{1}{2}}$$

Then

$$\begin{aligned} \vec{J}_m &= 2(-\frac{F}{\Delta}\hat{\rho}_m + \frac{F_\theta}{\Delta}\hat{\theta}_m)(H_\theta\hat{\theta_m} + H_\phi\hat{\phi_m})\frac{e^{-jk\rho_m}}{\rho_m}(\frac{\epsilon_0}{\mu_0})^{\frac{1}{2}} \\ &= 2(-\frac{F}{\Delta}H_\theta\hat{\phi_m} + \frac{F_\theta}{\Delta}H_\phi\hat{\theta}_m + \frac{F_\theta}{\Delta}H_\phi\acute{\rho_m})\frac{e^{-jk\rho_m}}{\rho_m}(\frac{\epsilon_0}{\mu_0})^{\frac{1}{2}} \end{aligned}$$

4.3.3 Radiated Field Patterns

In the far field, the radiated field of the main reflector can be calculated by:

$$\vec{E}(p) = -\frac{j\omega\mu_0}{4\pi}\int\int_s [\vec{J}_m - (\vec{J}_m \cdot \hat{R}_p)\hat{R}_p]\frac{e^{jkr}}{r}dS$$

Since the observation point P is very far away from the main reflector (see Figure 4.3) and using the analysis given in *Appendix B*, the following approximations are valid:

$$\begin{aligned} r &\approx R_p - \rho_m \sin\theta_m \sin\theta_p \cos(\phi_m - \phi_p) - \rho_m \cos\theta_m \cos\theta_p & (4.18) \\ \frac{e^{jkr}}{r} &\approx \frac{1}{R_p}[e^{-jkR_p} \cdot e^{jk\rho_m \sin\theta_m \sin\theta_p \cos(\phi_m - \phi_p)} \cdot e^{jk\rho_m \cos\theta_m \cos\theta_p}] & (4.19) \end{aligned}$$

In the far field, the $\dot{R}_p$ component vanishes. Using eq.(4.17) , eq.(4.18) , and the identities given in *Appendix C*, we can get

$$\begin{aligned} \vec{E}(p) \cdot \hat{\theta}_p = & -\frac{jk}{2\pi} \cdot \frac{e^{-jkR_p}}{R_p} \int\int_s e^{jk\rho_m \sin\theta_m \sin\theta_p \cos(\phi_m - \phi_p)} \cdot e^{-jk\rho_m(1-\cos\theta_m \cos\theta_p)} \\ & \cdot[FH_\theta \cos\theta_p \sin(\phi_m - \phi_p) + FH_\phi \cos\theta_m \cos\theta_p \cos(\phi_m - \phi_p) \\ & +FH_\phi \sin\theta_m \sin\theta_p + F_\theta H_\phi \sin\theta_m \cos\theta_p \cos(\phi_m - \phi_p) \\ & -F_\theta H_\phi \sin\theta_p \cos\theta_m] \sin\theta_m d\theta_m d\phi_m \\ \vec{E}(p) \cdot \hat{\phi}_p = & -\frac{jk}{2\pi} \cdot \frac{e^{-jkR_p}}{R_p} \int\int_s e^{jk\rho_m \sin\theta_m \sin\theta_p \cos(\phi_m - \phi_p)} \cdot e^{-jk\rho_m(1-\cos\theta_m \cos\theta_p)} \\ & \cdot[-FH_\theta \cos(\phi_m - \phi_p) + FH_\phi \cos\theta_m \sin(\phi_m - \phi_p) \\ & +F_\theta H_\phi \sin\theta_m \sin(\phi_m - \phi_p)] \sin\theta_m d\theta_m d\phi_m \end{aligned}$$

As shown before, for a vertical or X-polarization, the scattered patterns of the subreflector can be written as:

$$\begin{aligned} H_\theta &= h_\theta(\theta_m) \sin\phi_m \\ H_\phi &= h_\phi(\theta_m) \cos\phi_m \end{aligned}$$

Putting these into $\vec{E}(p)$ expressions and also use the integration identities described in *Appendix D*, the final $\vec{E}(p)$ field will be given as:

$$\vec{E}(p) \cdot \hat{\theta}_p$$

$$
\begin{aligned}
&= -\frac{jk}{2}\cdot\frac{e^{-jkR_p}}{R_p}\cos\phi_p\cdot\int_{\theta_m} e^{-jk\rho_m(1-\cos\theta_m\cos\theta_p)}\cdot\sin\theta_m \\
&\quad \cdot\{Fh_\theta\cos\theta_p[J_0(x_m)+J_2(x_m)] \\
&\quad +(Fh_\phi\cos\theta_m\cos\theta_p+F_\theta h_\phi\sin\theta_m\cos\theta_p)[J_0(x_m)-J_2(x_m)] \\
&\quad +2j(Fh_\phi\sin\theta_p\sin\theta_m-F_\theta h_\phi\sin\theta_p\cos\theta_m)J_1(x_m)\}d\theta_m \qquad (4.20)
\end{aligned}
$$

$$
\begin{aligned}
&\vec{E}(p)\cdot\hat{\phi}_p \\
&= \frac{jk}{2}\cdot\frac{e^{-jkR_p}}{R_p}\sin\phi_p\cdot\int_{\theta_m} e^{-jk\rho_m(1-\cos\theta_m\cos\theta_p)}\cdot\sin\theta_m \\
&\quad \cdot\{Fh_\theta[J_0(x_m)-J_2(x_m)] \\
&\quad +(Fh_\phi\cos\theta_m+F_\theta h_\phi\sin\theta_m)[J_0(x_m)+J_2(x_m)]\}d\theta_m \qquad (4.21)
\end{aligned}
$$

where $x_m = k\rho_m\sin\theta_m\sin\theta_p$.

4.4 Dual Shaped Reflector Antenna Performance

4.4.1 Gain

For a vertically polarized source, the radiation pattern of the main reflector can be expressed as:

$$\vec{E}(p) = -\frac{jk}{2}\cdot\frac{e^{-jkR_p}}{R_p}[M_\theta(\theta_p)\cos\phi_p\hat{\theta}_p - M_\phi(\theta_p)\sin\phi_p\hat{\phi}_p]$$

The electric field from the feed and subreflector is expressed as:

$$\vec{E}_{fs} = \frac{e^{-jkR_p}}{R_p}[E_\theta^{fs}(\theta_p)\cos\phi_p\hat{\theta}_p - E_\phi^{fs}(\theta_p)\sin\phi_p\hat{\phi}_p]$$

The total radiated electric field is given by:

$$
\begin{aligned}
\vec{E}_T &= \vec{E}(p)+\vec{E}_{fs} \\
&\quad \{[E_\theta^{fs}(\theta_p)-\frac{jk}{2}M_\theta(\theta_p)]\cos\phi_p\hat{\theta}_p
\end{aligned}
$$

$$
\begin{aligned}
&-[E_\phi^{fs}(\theta_p) - \frac{jk}{2}M_\phi(\theta_p)]\sin\phi_p\hat{\phi}_p\} \cdot \frac{e^{-jkR_p}}{R_p} \\
= \; & [S_\theta(\theta_p)\cos\phi_p\hat{\theta}_p - S_\phi(\theta_p)\sin\phi_p\hat{\phi}_p] \cdot \frac{e^{-jkR_p}}{R_p}
\end{aligned}
$$

where

$$
\begin{aligned}
S_\theta(\theta_p) &= E_\theta^{fs}(\theta_p) - \frac{jk}{2}M_\theta(\theta_p) \\
S_\phi(\theta_p) &= E_\phi^{fs}(\theta_p) - \frac{jk}{2}M_\phi(\theta_p)
\end{aligned}
$$

The co-polarized component can be obtained by:

$$E_c = [S_\theta(\theta_p)\cos^2\phi_p + S_\phi(\theta_p)\sin^2\phi_p] \cdot \frac{e^{-jkR_p}}{R_p}$$

The cross-polarized component can be expressed as:

$$E_X = [S_\theta(\theta_p) - S_\phi(\theta_p)]\sin\phi_p\cos\phi_p \cdot \frac{e^{-jkR_p}}{R_p} \tag{4.22}$$

The power gain of the antenna is defined by

$$G = \frac{P(\theta,\phi)}{P_T/4\pi}$$

where P_T is the total power radiated from feed. $P(\theta,\phi)$ is the power radiated per unit solid angle in the direction (θ,ϕ) and can be calculated by

$$P(\theta,\phi) = \frac{1}{2}(\frac{\epsilon_0}{\mu_0})^{\frac{1}{2}}R_p^2|E_c|^2$$

Then

$$G = \frac{2\pi(\frac{\epsilon_0}{\mu_0})^{\frac{1}{2}}|S_\theta(\theta_p)\cos^2\phi_p + S_\phi(\theta_p)\sin^2\phi_p|^2}{P_T} \tag{4.23}$$

The on-axis or boresight gain is obtained by set $\theta_p = 0, \phi_p = 0$ in eq.(4.22)

$$G|_{on-axis} = \frac{2\pi(\frac{\epsilon_0}{\mu_0})^{\frac{1}{2}}|S_\theta(0)|^2}{P_T}$$

The total power transmitted by feed P_T is derived in *Appendix E* and is expressed by

$$P_T = \frac{\pi}{2Z_0}\int_0^\pi (|g_\theta|^2 + |g_\phi|^2)\sin\theta d\theta$$

where Z_0 is the free space characteristic impedance.

4.4.2 Efficiency

For an aperture antenna, the boresight gain is given by [3], [55]

$$G = G_{max}\eta = \frac{4\pi A}{\lambda^2}\eta = [\frac{\pi D}{\lambda}]^2\eta$$

where A is the aperture area. D is the diameter of the circular aperture, and η is the antenna efficiency which can generally be partitioned as:

$$\eta = \eta_{ss}\eta_{sm}\eta_b\eta_A$$

In the above expression, $(1 - \eta_{ss})100$ represents the percentage of the power loss due to the energy from the feed past the subreflector. $(1 - \eta_{sm})100$ represents the percentage of the power loss due to the energy scattered from the subreflector past the main reflector. $(1 - \eta_b)100$ represents the percentage of the power loss caused by the feed, the subreflector blockage and the supporting struts. $(1 - \eta_A)100$ is the aperture efficiency, which represents the percentage of the power loss due to the remaining reasons which will be discussed later.

(a) Subreflector spillover efficiency (η_{ss})

The subreflector spillover efficiency (η_{ss}) is the power ratio between power subtended by subreflector to the total power radiated by the feed. The power loss due to the power from the feed past the subreflector, will usually contribute to the antenna sky noise. By this definition, the subreflector spillover efficiency can be calculated as:

$$\eta_{ss} = \frac{\int_0^{\theta_0}(|g_\theta|^2 + |g_\phi|^2)\sin\theta d\theta}{\int_0^{\pi}(|g_\theta|^2 + |g_\phi|^2)\sin\theta d\theta}$$

where θ_0 is the subreflector subtended angle. g_θ and g_ϕ are the components of the feed radiation pattern described before.

(b) Main reflector spillover efficiency (η_{sm})

The main reflector spillover efficiency (η_{sm}) is the power ratio between power subtended by main reflector to the power scattered by the subreflector. If the subreflector surface has no loss, the scattered power is equal to the power subtented by the subreflector. If the main reflector subtanded angle is θ_{m_0}, then the main reflector spillover efficiency is given by

$$\eta_{sm} = \frac{\int_0^{\theta_{m_0}}(|h_\theta|^2 + |h_\phi|^2)\sin\theta d\theta}{\int_0^{\theta_0}(|g_\theta|^2 + |g_\phi|^2)\sin\theta d\theta}$$

where h_θ and h_ϕ are defined in eq.(4.15) and eq.(4.16).

(c) Subreflector blockage efficiency (η_b)

If the supporting strut blockage is ignored, then the main blockage effect comes only from the subreflector. Hence, the subreflector blockage efficiency can be calculated by the gain ratio between the on-axis gain with subreflector blockage to the on-axis gain without blockage, i.e.,

$$\eta_b = \frac{G|_{on-axiswithblockage}}{G|_{on-axiswithoutblockage}}$$

(d) Aperture efficiency (η_A)

After having obtained η_{ss}, η_{sm} and η_b, then by definition, the aperture efficiency is given by:

$$\eta_A = \frac{G}{G_{max}\eta_{ss}\eta_{sm}\eta_b} = \frac{\eta}{\eta_{ss}\eta_{sm}\eta_b}$$

where G is the antenna boresight gain.

In the above evaluation, the aperture efficiency can further be subdivided as follows [58]:

$$\eta_A = \eta_p\eta_i\eta_x\eta_r$$

where $(1-\eta_p)100$ represents the percentage of the power loss which arises if the field over the aperture is not everywhere in phase. $(1-\eta_i)100$ represents the percentage of the power loss due to the non-uniformity of the amplitude of the aperture illumination. $(1-\eta_x)100$ represents the percentage of the power loss caused if there are cross-polarized fields present in the antenna aperture. $(1-\eta_r)100$ represents the percentage of the power loss due to the random error over the reflector surfaces caused by mechanical defects.

4.5 Numerical Results and Comparison

Based on the PO theory, a computer-aided analysis program is developed. Then the scattered patterns of subreflector and the radiation patterns of main reflector can be calculated. Thus, any parameter of the antenna specifications can be studied and optimized. However, the validity of the PO method should be verified.

4.5.1 Comparison with Experimental results

An experiment called *Scattering from hyperboloidal reflector* was carried out by *W.V.T.Rusch* [53] in *1963*. In this experiment, he used a feed horn to illuminate a hyperboloidal reflector, and then measured the scattered pattern from the hyperboloid reflector. Refer to Figure 4.4(a), the hyperboloidal reflector profile can be written as:

$$\rho = -\frac{ep}{1+e\cos\theta}, \qquad (\theta_0 \le \theta \le \pi)$$

where

$$e = \frac{c}{a}$$

$$p = c(1-\frac{1}{e^2}).$$

The measured feed pattern given by *W.V.T.Rusch* [53] is shown in Figure 4.5. The measured H-Plane scattered pattern and our calculated pattern are shown in Figure 4.6. The agreement is good except in the center region because the experimental pattern is distorted by the feed horn blockage which was not included in the calculation.

4.5.2 Subreflector Scattered Patterns

The scattered patterns of the subreflector related to the profiles and structures shown in Figure 3.4, Figure 3.5, Figure 3.7, and Figure 3.8 are given in Figure 4.7, Figure 4.8, Figure 4.9, and Figure 4.10. The feed radiation pattern is plotted and shown in Figure 3.4. The operation frequency is $14.25GHz$.

4.5.3 Antenna Radiation Patterns

The close-in($\theta < 2^o$) and far-angle radiation patterns of the antenna related to the profiles and structures shown in Figure 3.4, Figure 3.5, Figure 3.7, and Figure 3.8 are given in Figure 4.11,Figure 4.12, Figure 4.13, Figure 4.14, Figure 4.15,Figure 4.16, Figure 4.17, and Figure 4.18. The operation frequency is $14.25GHz$. The

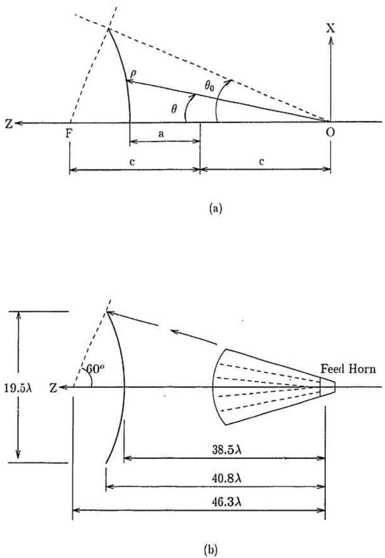

Figure 4.4: The geometry of the experimental set-up. (a) the hyperboloidal reflector and the coordinate system (b) the geometry of the experimental set-up ($f = 9.6GHz$)

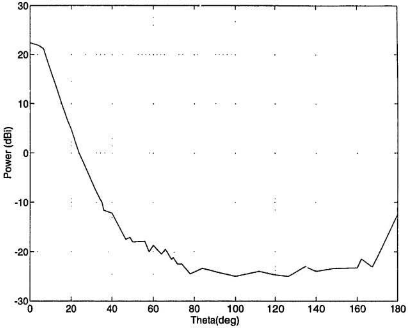

Figure 4.5: The measured feed horn pattern in [53]

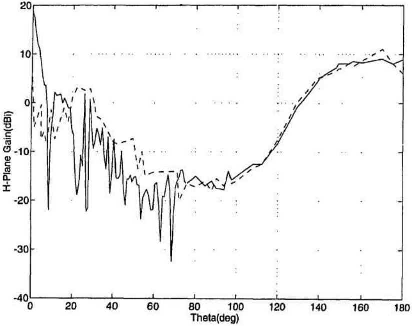

Figure 4.6: The measured and the calculated *H*-Plane Scattered patterns. Solid line: Calculated Dotted line: Envelop of the measured data

CCITT specifications are also included. By using the 3-dimensional view, the E-Plane pattern illustrated in Figure 4.12 is also redrawn and shown in Figure 4.19. We can see that the main beam of dual shaped reflector antenna radiation pattern is very sharp and the boresight gain is very high.

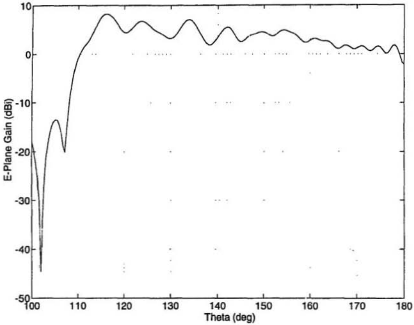

Figure 4.7: Scattered pattern of subreflector for Cassegrain antenna (the feed radiation pattern shown in Figure 3.4, the main and subreflector profiles shown in Figure 3.5.)

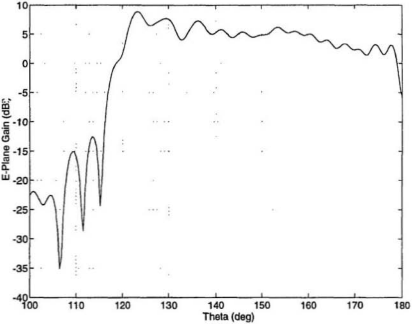

Figure 4.8: Scattered pattern of subreflector for Cassegrain antenna (the feed radiation pattern shown in Figure 3.4, the main and subreflector profiles shown in Figure 3.6.)

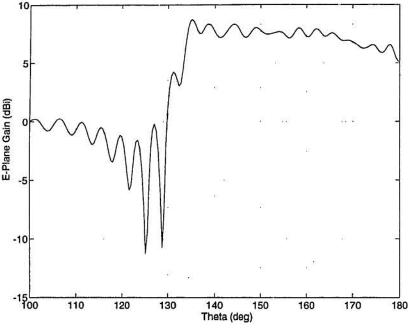

Figure 4.9: Scattered pattern of subreflector for Gregorian antenna (the feed radiation pattern shown in Figure 3.4, the main and subreflector profiles shown in Figure 3.9.)

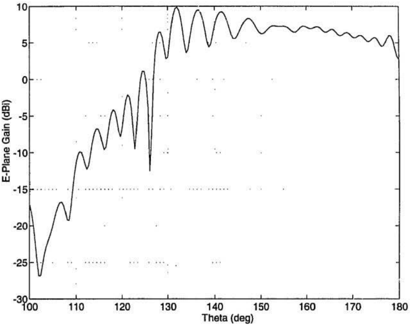

Figure 4.10: Scattered pattern of subreflector for Gregorian antenna (the feed radiation pattern shown in Figure 3.4, the main and subreflector profiles shown in Figure 3.10.)

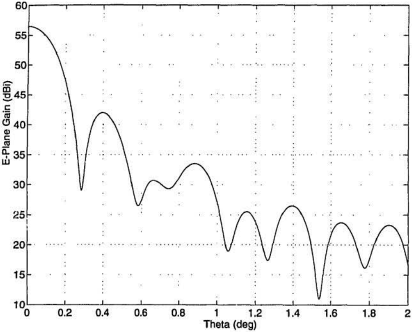

Figure 4.11: Close-in radiation pattern of main reflector for Cassegrain antenna (the scattered pattern of subreflector shown in Figure 4.7, the main and subreflector profiles shown in Figure 3.5.)

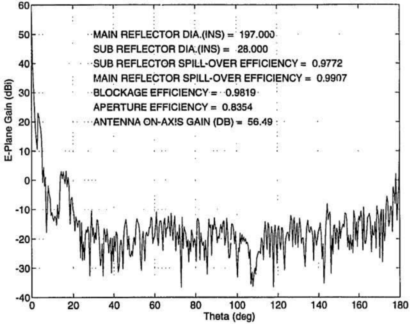

Figure 4.12: Far-angle radiation pattern of main reflector for Cassegrain antenna (the scattered pattern of subreflector shown in Figure 4.7, the main and subreflector profiles shown in Figure 3.5.)

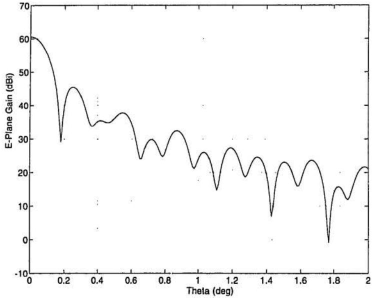

Figure 4.13: Close-in radiation pattern of main reflector for Cassegrain antenna (the scattered pattern of subreflector shown in Figure 4.8, the main and subreflector profiles shown in Figure 3.6.)

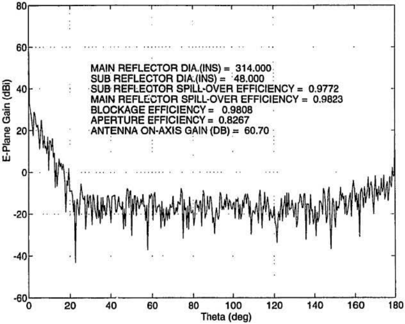

Figure 4.14: Far-angle radiation pattern of main reflector for Cassegrain antenna (the scattered pattern of subreflector shown in Figure 4.8, the main and subreflector profiles shown in Figure 3.6.)

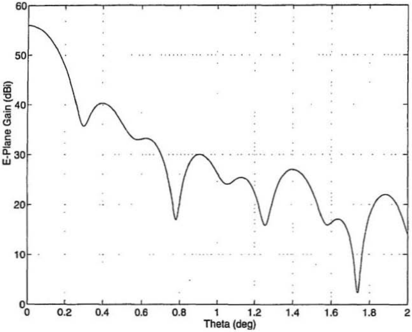

Figure 4.15: Close-in radiation pattern of main reflector for Gregorian antenna (the scattered pattern of subreflector shown in Figure 4.9, the main and subreflector profiles shown in Figure 3.9.)

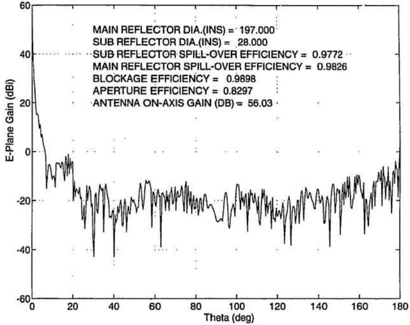

Figure 4.16: Far-angle radiation pattern of main reflector for Gregorian antenna (the scattered pattern of subreflector shown in Figure 4.9, the main and subreflector profiles shown in Figure 3.9.)

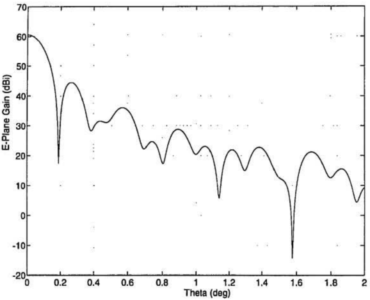

Figure 4.17: Close-in radiation pattern of main reflector for Gregorian antenna (the scattered pattern of subreflector shown in Figure 4.10, the main and subreflector profiles shown in Figure 3.10.)

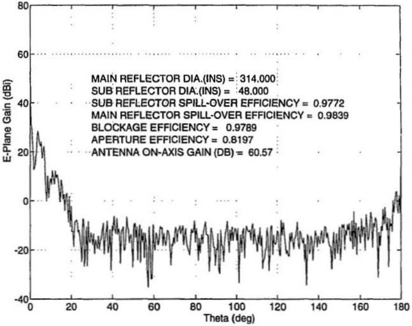

Figure 4.18: Far-angle radiation pattern of main reflector for Gregorian antenna (the scattered pattern of subreflector is shown Figure 4.10, the main and subreflector profiles shown in Figure 3.10.)

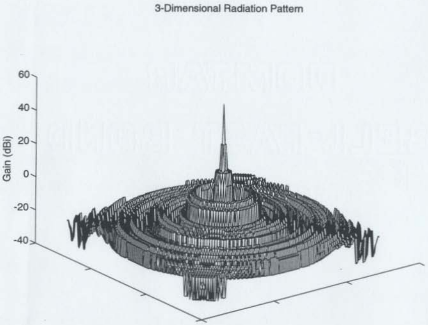

Figure 4.19: 3-Dimensional radiation pattern (The E-Plane radiation pattern plotted in Figure 4.12).

Chapter 5

Dual Shaped Reflector Antenna Performance Trade-offs and Comparison

Based on the theories presented in the previous chapters, the dual shaped reflector antennas can be designed and analyzed. However, with the continuing expansion in microwave communication systems, particularly in areas of population concentration, the sidelobe level must strictly be controlled to prevent the probability of interferences. In addition, a high sidelobe level also means an increase in noise temperature, especially for low noise antennas used in earth stations. The power loss passed the main reflector will contribute to the ground noise. This noise is normally much greater than the sky noise. Therefore, the final designed antenna is required to meet the CCITT specifications, especially to prevent interferences with other systems. Thus, the power pattern control is a very important issue in earth-station antenna designs. In this chapter, the trade-offs between antenna performances and the main reflector aperture power distributions are investigated and a power pattern control method is presented. The performances of Cassegran and Gregorian antennas are also compared.

5.1 Dual Shaped Reflector Antenna Performance Trade-Offs

The principal advantage of dual reflector antennas is to improve the gain or sidelobes by shaping the reflectors with different kinds of reflector aperture power distributions[25] [26] [30] [43] [44] [45] [46]. Because of the simplicity and the realizability, Gaussian distribution is used in this thesis.

5.1.1 Gaussian Distribution on the Antenna Aperture

It is well known that the maximum boresight gain can be achieved with uniform aperture power distribution. However, the sidelobe levels are often to high to meet the CCITT specification, and the high power density at the main reflector edge will produce high spillover. Thus, the power distribution on the main reflector aperture should be varied from uniform distribution to a kind of non-uniform distribution [43] [44] [45] [46] in which the power density on the edge is gradually tapered to within $-10dB$ to $-15dB$. Due to the sub-reflector blockage, there will be no power at the central area of main reflector aperture, but we also assume that the power distribution at the edges of the subreflector is gradually tapered.

Making use of the revolutional axis, the power density, P_A, can be expressed as the function of positions on the main reflector aperture, ρ:

$$\begin{aligned} P_A &= 1 & (\rho_{m_1} \le \rho \le \rho_{m_2}) \\ P_A &= exp\{-b_2 \cdot (\frac{\rho - \rho_{m_2}}{\rho_{max} - \rho_{m_2}})^2\} & (\rho_{m_2} \le \rho \le \rho_{max}) \\ P_A &= exp\{-b_1 \cdot (\frac{\rho_{m_1} - \rho}{\rho_{m_1}})^2\} & (0 \le \rho \le \rho_{m_1}) \end{aligned}$$

where ρ_{max} is the radius of main reflector aperture. ρ_{m_1} and ρ_{m_2} are the lower

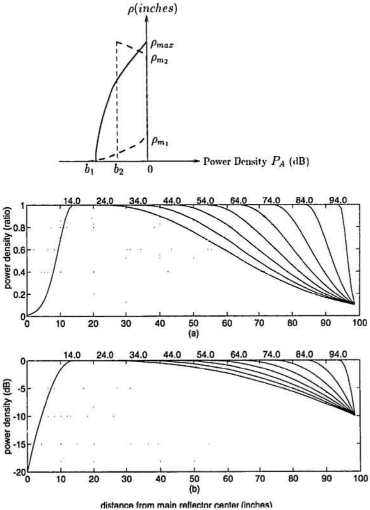

Figure 5.1: Power distribution on the main reflector aperture

and upper limited positions of uniform power distribution area, as shown in Figure 5.1. b_1 is the aperture power density at center of the main reflector aperture. b_2 is the aperture power density at the edge of the main reflector. For the main reflector with radius 98.5″, using $b_1 = -20dB$, $b_2 = -10dB$ and $\rho_{m_1} = 14.0''$, the power distributions on the main reflector aperture with different ρ_{m_2} are shown in Figure 5.1.

5.1.2 Gain and Sidelobe Versus Aperture Distributions

With Gaussian aperture power distributions, the dual shaped reflector antenna is designed and analyzed. The trade-offs between gain, sidelobes, aperture efficiencies and different aperture power distributions can be investigated. For a Cassgrain antenna with the main reflector radius of 98.5″, and the subreflector radius of 9.0″, the feed radiation pattern shown in Figure 3.4 and the phase center is located on the z axis at 27″ behind the main reflector aperture (refer to Figure 3.3), the near-in (within 1.0°) radiation patterns related to different aperture power distributions are shown in Figure 5.2.

It can be seen from Figure 5.2 that shaping for a given aperture power distribution other than a uniform one helps to achieve two goals. First, the spillover past the main reflector can be substantially reduced and this in turn reduces the noise temperature of the antenna system. Secondly, the non-uniform aperture distribution can reduce the sidelobe levels as expected. On the other hand, the non-uniform aperture distribution results in the loss of gain and the broader beamwidth. The smaller the uniform distribution area, the less the gain, the lower the sidelobe levels and the broader the beamwidth. However, the gain loss due to the non-uniform

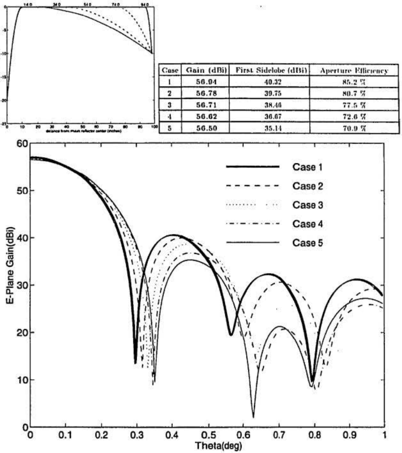

Case	Gain (dBi)	First Sidelobe (dBi)	Aperture Efficiency
1	56.94	40.32	85.2 %
2	56.78	39.75	80.7 %
3	56.71	38.46	77.5 %
4	56.62	36.67	72.6 %
5	56.50	35.14	70.9 %

Figure 5.2: Radiation patterns. $\rho_{max} = 98.5''$, $\rho_{m_1} = 10.0''$, $\rho_{m_2} = 94.0''$, $74.0''$, $54.0''$, $34.0''$, $14.0''$, $b_1 = -20dB$, $b_2 = -10dB$

aperture power distribution is not distinguishable compared to the decreasing of sidelobe levels. Thus, the non-uniform aperture power distribution provides us a means to control the sidelobes of the dual shaped reflector antennas.

As demonstrated in Figure 5.3 and Figure 5.4, the sidelobes of the antenna designed based on the aperture power distribution of *Case 1* shown in Figure 5.2 does not meet the CCITT specification, which is

$$32 - 25log(\theta) \quad (\theta \text{ in } degrees)$$

By using the aperture power distribution of *Case 4* shown in Figure 5.2, the sidelobes of the designed antenna are reduced, consequently they meet the CCITT specification.

5.2 Comparison of Cassegrain and Gregorian Antennas

The main difference between Cassgrain and Gregorian antennas is the shape of subreflectors. One has a hyperboloidal subreflector and the other has a ellipsoidal subreflector. In reality, most symmetrical dual reflector antennas are of Cassgrain type. However, in some special cases, for example, in the heavy snowing environment, the Gregorian types are used to prevent snow from covering the reflecting surface of the subreflector. In order to provide other reasons, the performances of these two kinds of antennas will be compared.

The radiation patterns of Cassegrain and Gregorian antennas are compared by using two different cases. In the first case, both Cassegrain and Gregorian antennas have the same feed pattern, phase center location, main and subreflector radii, subreflector subtended angle and the same main reflector power distribution,

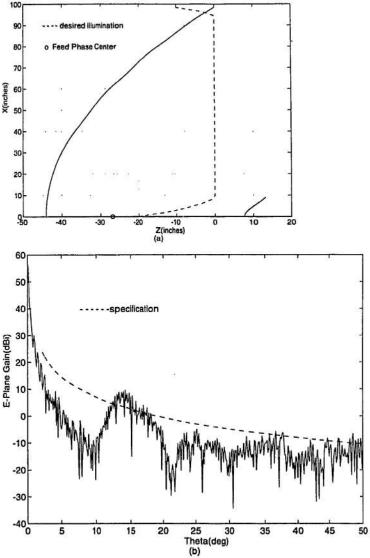

Figure 5.3: Antenna profile and radiation pattern. $\rho_{max} = 98.5''$, $\rho_{m_1} = 10.0''$, $\rho_{m_2} = 94.0''(Case1)$, $b_1 = -20dB, b_2 = -10dB$

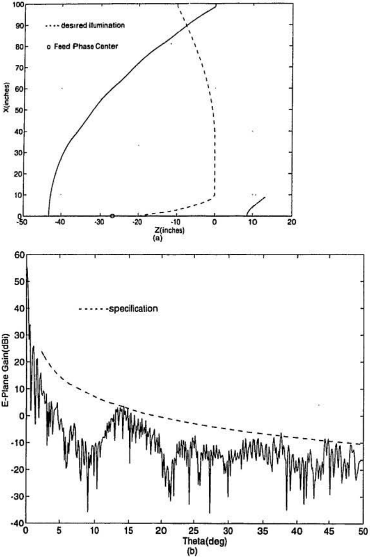

Figure 5.4: Antenna profile and radiation pattern.$\rho_{max} = 98.5''$, $\rho_{m_1} = 10.0''$, $\rho_{m_2} = 34.0''(Case4)$, $b_1 = -20dB, b_2 = -10dB$

as shown in Figure 5.5. The close-in and far-angle radiation patterns of Cassegrain and Gregorian antennas are shown in Figure 5.6 and 5.7 respectively. In the second case, both Cassegrain and Gregorian antennas have the same feed pattern, main and subreflector radii, subreflector subtended angle and the same main reflector power distribution, but different phase center locations, as shown in Figure 5.8. The close-in and far-angle radiation patterns of Cassegrain and Gregorian antennas are shown in Figure 5.9 and 5.10 respectively.

It can be seen that in both cases, the close-in radiation patterns and the far-angle radiation patterns of Cassegrain and Gregorian antennas are almost the same. Because of the same main reflector power distribution, the antenna aperture efficiencies for both Cassegrain and Gregorian antenna are the same. But there are still some differences stated as follows:

(a) The close-in sidelobes of the Gregorian antennas are smaller than those of Cassegrain antennas.

(b) The back radiations (near 180°) of Gregorian antennas are higher than that of Cassegrain antennas.

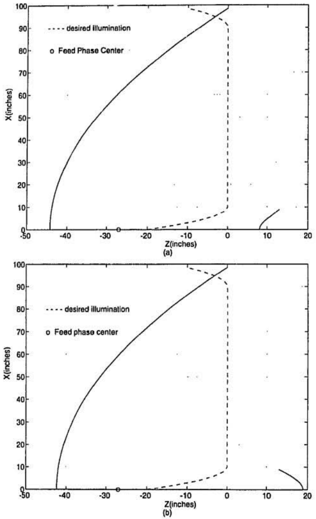

Figure 5.5: Cassegrain and Gregorian antennas with the same feed pattern (Figure 3.4), phase center location($-27''$), main reflector radius ($98.5''$), subreflector radius($9.0''$), subreflector subtended angle (12.7°)and the same main reflector power distribution. (a)Cassegrain antenna (b) Gregorian antenna

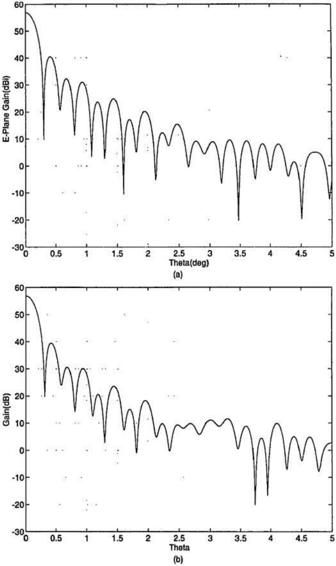

Figure 5.6: Close-in radiation patterns of (a) Cassegrain antenna and (b) Gregorian antenna for the configurations shown in Figure 5.5

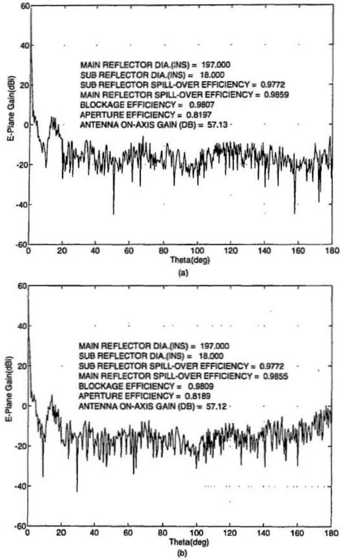

Figure 5.7: Far-angle radiation patterns of (a) Cassegrain antenna and (b) Gregorian antenna for the configurations shown in Figure 5.5

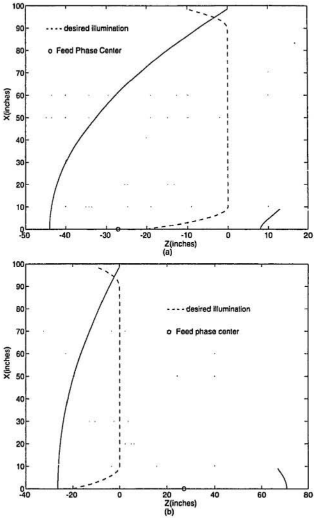

Figure 5.8: Cassegrain and Gregorian antennas with the same feed pattern (Figure 3.4), main reflector radius (98.5″), subreflector radius(9.0″), subreflector subtended angle (12.7°) and the same main reflector power distribution, but different phase center locations(−27″ for Cassgrain antenna, 27″ for Gregorian antenna) (a) Cassegrain antenna (b) Gregorian antenna

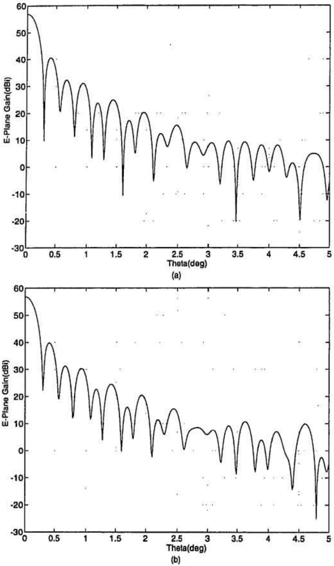

Figure 5.9: Close-in radiation patterns of (a) Cassegrain antenna and (b) Gregorian antenna for the configurations shown in Figure 5.8

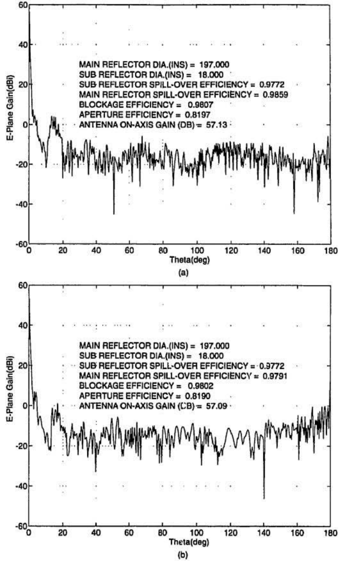

Figure 5.10: Far-angle radiation patterns of (a) Cassegrain antenna and (b) Gregorian antenna for the configurations shown in Figure 5.8

Chapter 6

Conclusion and Future Work

In satellite communications, the pencil beam antenna plays an important role in the vital link between the earth station and the satellite repeater due to its high boresight gains. And as the continuing expansion of satellite communications has led to more earth stations and more satellite repeaters, the possibility of interference between one and another increases, most of all the possible interference between channels due to the frequency reuse. The control of sidelobe levels and the cross-polarization discrimination are, of course, the major concerns of the antenna designers and also are the essential problems to be solved in this thesis.

The thesis began with the basic theory behind the hybrid mode feed horns in chapter 2 to show that only the corrugated born can, in practice, approaches the ideal conditions, which are identical electric and magnetic field patterns, extremely low cross- polarization and well defined phase center.

In the past, the dual reflectors of an axial-rotationally symmetric system have been constrained by either the hyperboloid-paraboloid (Cassegrain antenna) or the ellipsoid-paraboloid (Gregorian antenna) combination. In order to obtain a uniform illumination on the antenna aperture for the maximum gain the designer has only the feed to optimize. When the feed has achieved an optimal design, no further improvements of the antenna performance could be realized. Now, as the advances of computer analyses . ave enabled the main and subreflectors, which had previously been considered as constraints, to be modified. Chapter 3 has clearly demonstrated that after having designed the feed, one can impose a desired illumination distribution on the antenna aperture and shape the reflectors such that the maximum gain or the sidelobe levels are achieved. The geometric optics approach has been used to set up 3 differential equations related to the surface profiles of main and subreflectors. The computer aided synthesis programs have developed to compute the non-closed form reflector profiles for both Cassegrainian and Gregorian antennas.

After generating the reflector profiles and by using the physical optics techniques, chapter 4 has shown step by step how to calculate the scattered patterns of the combined feed and subreflector, then the radiation patterns of the whole antenna as well as the entire antenna specifications. The combination of the developed softwares in both chapters 3 and 4 has manifested itself in two essential applications. One is to upgrade the performance of the existing earth stations where both closed form profiles were used. In these systems, the antenna efficiency is about 50 to 60 percent. To upgrade the performance up to 75 to 80 percent, the feed and subreflector can be redesigned while the main reflector is retained due to the fact that it is quite costly to replace. The other is to design a brand new antenna in which both reflectors and feed are fully optimized. In addition, the validity of the physical optics was also verified in chapter 4. Chapter 5 devoted to the development of the pattern control method. This made the software package extremely useful in the design of pencil beam antennas for all large earth stations.

For a given specification, this software package can be used to design the feed horn, reflector profiles and the whole antenna structure with the optimal performance in both mechanical and electrical specifications. It is important to note that normally a design house such as SPAR Aerospace Limited is in favor of Cassegrain antennas, while ANDREW Antenna Company Limited is in favor of Gregorian antennas. There is no one who has both Cassegrain and Gregorian designs. Here, this design software package provides designers with both Cassegrain and Gregorian choices. The comparison between Cassegrain and Gregorian antennas have been given in chapter 5 to demonstrate that depending upon the requirements, one can be better used than the other.

Finally the main contribution of this research can be summarized as follows:

Although the Gregorian antennas have existed in many applications, the sophisticated computer aided design and analysis have not been reported. Furthermore there has not been a complete computer aided design and synthesis softwares of this nature for both Cassegrainian and Gregorian antennas. This package provides the designers vital tools to design and analyse both the existing and future large earth stations.

In this thesis, the complete computer aided design and analysis software of the dual shaped reflector antenna for earth stations have been developed based on the geometric optics and physical optics, which are valid for large earth stations. For small earth stations, the dimension of the antenna is becoming compatible with the operating wavelength, these approaches are no longer valid. The *Geometrical Theory of Diffraction* (GTD) must be used. The reflector edge diffraction will be added into the scattered patterns and radiation patterns to improve the accuracy of the calculations. GTD will also be used to modify GO in the design of the reflectors. In addition, the effects of supporting struts of the subreflector should be taken into account with respect to the gain reduction and the sidelobe levels. Last but not least, the noise performance will be added in the analysis software. It is hoped that our computer aided software will provide an efficient tool in the design as well as the analysis of dual shaped reflector antennas.

Bibliography

[1] John F. Ramsay, *Microwave Antenna and Waveguide Techniques Before 1900*. Proc. IRE, vol.46(2), pp.405-415, 1958.

[2] G. Reber, *Cosmic Static*, Astrophys. J., vol.103(3), pp.279-287, 1944.

[3] S. Silver, *Microwave Antenna Theory and Design*, McGraw-Hill, New York, 1949.

[4] R.H. Brown and A.C.B. Lovell, *The Exploration of Space by Radio*, John Wiley, New York, 1957.

[5] C.C. Cutler, *Parabolic Antenna Design for Microwaves*, Proc. IRE, vol.35(11), pp.1284-1294, 1947.

[6] E.M.T. Jones, *Paraboloid Reflector and Hyperboloid Lens Antennas*, IRE Trans. Antennas Propagat., AP-2(4), pp.119-127, 1954.

[7] I. Koffman, *Feed Polarization for Parallel Currents in Reflectors Generated by Conic Sections*, IEEE Trans. Antennas Propagat., AP-14(1), pp.37-40, 1966.

[8] P.W. Hannan, *Microwave Antennas Derived from the Cassegrain Telescope*, IRE Trans. Antenna Propagat., AP-9(2), pp.140-153, 1961.

[9] B.Ye. Kinber, *On Two Reflector Antennas*, Radio Eng. Electron. Phys., vol.7(6), pp.914-921, 1962.

[10] S.P. Morgan, *Some Examples of Generalized Cassegrainian and Gregorian Antennas*, IEEE Trans. Antennas Propagat., AP-12(6), pp.685-691, 1964.

[11] P.D. Potter, W.D. Merrick and A.C. Ludwig, *Big Antenna systems for Deep-Space Communications*, Astronautics and Aeronautics, Oct., pp.84-95, 1966.

[12] V. Galindo, *Design of Dual-Reflector Antennas with Arbitrary Phase and Amplitude Distributions*, IEEE Trans. Antennas Propagat., AP-12(4), pp.403-408, 1963.

[13] W.F. Williams, *High Efficiency Antenna Reflector*, Microwave J., vol.8(7), pp.79-82, 1965.

[14] P.D. Potter, *A New Horn Antenna with Suppressed Sidelobes and Equal Beamwidths*, Microwave J., vol.6(6), pp.71-78, 1963.

[15] P.D. Potter and A.C. Ludwig, *Beamshaping by use of higher order modes in conical horns*, NEREM Record 1963, vol.5, pp.92-93, Northeast Electronics Research and Engineering Meeting, Boston, Mass.

[16] A.F. Kay, *The Scalar Feed*, AFCRL Rep

[17] H.C. Minnett and B.MacA. Thomas, *A Method of Synthesizing Radiation Patterns with Axial Symmetry*, IEEE Trans. Antennas Propagat., AP-14(5), pp654-656, 1966.

[18] H.C. Minnett and B.MacA. Thomas, *Fields in the Image Space of Symmetrical Focusing Reflectors*, Proc. IEE, vol.115, pp.1419-1430, Oct., 1968.

[19] V.H. Rumsey, *Horn Antennas with Uniform Power Patterns Around Their Axes*, IEEE Trans. Antennas Propagat., AP-14(5), pp.656-658, 1966.

[20] R.E. Lawrie and L.Peters, *Modifications of Horn Antennas for Low Sidelobe Levels*, IEEE Tran. Antennas Propagat., AP-14(5), pp.605-610, 1966.

[21] M.E.J. Jeuken, *Exprimental Radiation Pattern of the Corrugated Conical Horn Antenna with Small Flare Angle*, Electro. Lett., vol.5(20), pp.484-485, 1969.

[22] M.S. Narasimhan and B.V. Rao, *Hybrid Modes in Corrugated Conical Horn*, Electron. Lett., vol.6(2), pp.32-34, 1970. 1990.

[23] P.J.B. Clarricoats and P.K. Saha, *Propagation and Radiation Behaviour of Corrugated feeds*,
Part 1: Corrugated-waveguide feed
Part 2: Corrugated-conical-horn feed,
Proc. IEE, vol.118(9), pp.1167-1186, 1971.

[24] J.J. Lee, L.I. Parad and R.S. Chu, *A Shaped Offset-fed Dual Reflector Antenna*, IEEE Trans. Antennas Propagat., vol. AP-27(2), pp.165-171, 1979.

[25] V. Galindo-Isreal, R. Mittra and A.G. Cha, *Aperture Amplitude and Phase Control of Offset Dual Reflectors*, IEEE Trans. Antennas Propagat., vol. AP-27(2), pp.154-164, 1979.

[26] C.J. Sletten, *Numerical Technique for Shaping Reflector Surfaces to Synthesize Antenna Patterns*, Proc. IEEE, vol. 69, No. 3, pp.392-394, 1981.

[27] A.R. Cherrette, S.W. Lee and R.J. Acosta, *A Method for Producing a Shaped Contour Radiation Pattern Using a Single Shaped Reflector and a Single Feed*, IEEE Trans. Antennas Propagat., vol. AP-37(6), pp.698-706, 1989.

[28] K. Shogen, H. Nishida and N. Toyama, *Single Shaped Reflector Antennas for Broadcasting Satellites*, IEEE Trans. Antennas Propagat., vol.40(2), pp. 178-187, 1992.

[29] V. Galindo-Isreal and R. Mittra, *Synthesis of Offset Dual Shaped Subreflector Antennas for Control of Cassegrain Aperture Distributions*, IEEE Trans. Antennas Propagat., vol. AP-32(1), pp. 86-92, 1984.

[30] V. Galindo-Isreal, W. Veruttipong, R.D. Norrod and W.A. Imbriale, *Scanning Properties of Large Dual-Shaped Offset and Symmetric Reflector Antennas*, IEEE Trans. Antennas Propagat., vol. AP-40(4), pp.422-432, 1992.

[31] B. Daveau, *Synthese et optimisation de reflecteurs de forme speciale pour antennes*, Rev. Tech. Thomson-CSF, vol.2(1), pp. 37-55, 1970.

[32] K.A. Green, *Modified Cassegrain Antenna for Arbitrary Aperture Illumination*, IEEE Trans. Antennas Propagat., vol. AP-11, pp.589-590, 1963.

[33] P.D. Potter, *Application of Spherical Wave Theory to Cassegrainian-fed Paraboloids*, IEEE Trans. Antennas Propagat., vol. AP-15, pp.727-736, 1967.

[34] P.J. Wood, *Field Correlation Theorem with Application to Reflector Aerial Diffraction Problem*, Electron. Letts., vol. 6, no. 11, pp.326-327, 1970.

[35] P.J. Wood, *Spherical Waves in Antenna Problems*, Marconi Rev., vol.34, No. 182, pp.149-172, 1971.

[36] P.J. Wood, *Reflector Profiles for the pencile-beam Cassegrain Antenna*, Marconi Rev., vol. 35, No.185, pp.121-138, 1972.

[37] G.L. James and G.T. Poulton, *Modified Diffraction Coefficients for Focussing Reflectors*, Electron. Letts., vol. 9, No. 23, pp.537-538, 1973.

[38] G.L. James, *Edge Diffraction at a Curved Screen*, Electron. Letts., vol. 10, No. 10, pp. 167-169, 1974.

[39] R.M. Lewis and J. Boersma, *Uniform Asympotic Theory of Edge Diffraction*, J. Math. Phys., vol. 10, pp.2291-2305, 1969.

[40] H.E. Bartlett and R.E. Mosely. *Dielguides-High efficiency Low Noise Antenna Feeds*, Microwave J., vol. 9, No. 12, pp. 2071-2102, 1969.

[41] P.J.B. Clarricoats and C.E.R.C. Salema, *Antennas Employing Conical Dielectric Horns, Part I-Propagation and Radiation Characteristics of Dielectric Cones, Part II-The Cassegrain Antenna*, Proc. IEE, vol. 120, pp.741-756, 1973.

[42] A.W.Rudge and N.A. Adatia, *Offset-Paraboloic Reflector Antennas: A Review*, Proc. IEEE, vol. 66(12), 1978.

[43] T.T. Taylor, *Design of Circular Apertures for Narrow Beamwidth and Low Sidelobe*, IRE Trans. Antennas Propagat., vol. AP-9, pp.17-22, 1960.

[44] R.C. Hansen, *A One-Parameter Circular Aperture Distribution with Narrow Beamwidth and Low Sidelobes*, IEEE Trans. Antennas Propagat., vol. AP-25, pp.477-480, 1976.

[45] A.C. Ludwig, *Low Sidelobe Aperture Distributions for Blocked and Unblocked Circular Aperture*, IEEE Trans. Antennas Propagat., vol. AP-30, pp.933-946, 1982.

[46] D. Duan and Y. Rahmat-Samii, *A Generalized Three-Parameter (3-P) Aperture Distribution for Antenna Applications*, IEEE Trans. Antennas Propagat., vol. AP-40, pp.697-713, 1992.

[47] P.J.B.Clarricoats and G.T.Poulton, *High-Efficiency Microwave Reflector Antenna - A Review*, Proc. IEEE, Vol.65(10), 1977.

[48] R.G. Kouyoumjian, *Asymptotic High Frequency Methods*, Proc. IEEE, vol. 53, pp.864-876, 1965.

[49] L.B. Felsen and N. Marcuvitz, *Radiation and Scattering of Waves*, Prentice-Hall, New Jersey, 1973.

[50] J. Keller, *Geometrical Theory of Diffraction*, J.Opt. Soc. Amer., vol. 52, pp.116-130, 1962.

[51] R.G. Kouyoumjian and P.H. Pathak, *A Uniform Geometrical Theory of Diffraction for an Edge in a Perfect Conducting Surface*, Proc. IEEE, vol. 62, pp.1448-1461, 1974.

[52] B.E. Kinber, *On Two Reflector Antennas*, Radio Engg. Electronic Phys., vol. 7, pp.914-921, 1962.

[53] W.V.T. Rusch, *Scattering from a Hyperboloidal Reflector in a Cassegrainian Feed System*, IEEE Trans. Antennas and Propagat., vol. AP-11(4), pp.414-421, 1963.

[54] P.J. Wood, *Reflector Antenna Analysis and Design*, Peter Peregrinus Ltd., UK, 1980.

[55] W.V.T. Rusch and P.D. Potter, *Analysis of Reflector Antennas*, Academic Press, New York, 1970.

[56] J.K.M. Jansen, M.E.J. Jenken and C.W. Lambrechtse,*The Scalar Feed*, AEU, vol. 26, pp.22-30, Jan., 1970.

[57] M.S. Narasimhan and B.V. Rao, *Diffraction by Wide- Flare-Angle Corrugated Conical Horns*, Electro. Lett., No. 10, pp.469-471, 1970.

[58] S. Le-Ngoc, *Design Aspects of Dual Reflector Antennas for Satellite Communication*, Engineering report No.352, Raytheon Canada Limited, May, 1979.

Appendix A

Expressing $\hat{\theta}_f$ in Subreflector Coordinate System

Refer to Figure 4.2, $\hat{\theta}_f$ can be expressed using $\hat{x}_f$, $\hat{y}_f$ and $\hat{z}_f$:

$$\hat{\theta}_f = \cos\theta_f \cos\phi_f \hat{x}_f + \cos\theta_f \sin\phi_f \hat{y}_f - \sin\phi_f \hat{y}_f$$

Because $\hat{x}_f = \hat{x}_s$, $\hat{y}_f = \hat{y}_s$, and $\phi_f = \phi_s$,

$$\begin{aligned} \hat{\theta}_f &= \cos\theta_f \cos\phi_s(\hat{\rho}_s \sin\theta_s \cos\phi_s + \hat{\theta}_s \cos\theta_s \cos\phi_s - \hat{phi}_s \sin\phi_s) \\ &\quad + \cos\theta_f \sin\phi_s(\hat{\rho}_s \sin\theta_s \sin\phi_s + \hat{\theta}_s \cos\theta_s \sin\phi_s + \hat{phi}_s \cos\phi_s) \\ &\quad - \sin\theta_f(\hat{\rho}_s \cos\theta_s - \hat{\theta}_t \sin\theta_s) \\ &= \sin(\theta_s - \theta_f)\hat{\rho}_s + \cos(\theta_s - \theta_f)\hat{\theta}_s \end{aligned}$$

Appendix B

Expressing $\frac{e^{-jkr}}{r}$ in Main reflector Coordinate System

Refer to Figure 4.2,

$$\begin{aligned} \vec{r} &= \hat{\rho}_m - \hat{\rho}_{sm} \\ r &= \vec{r}\cdot\hat{r} = \rho_m\hat{\rho}_m\cdot\hat{r} - \rho_{sm}\hat{\rho}_{sm}\cdot\hat{r} \end{aligned}$$

If O_m is close to subreflector and $M(\rho_m, \theta_m, \phi_m)$ is far away from subreflector, then $\hat{\rho}_m \approx \hat{r}$ and $\rho_m \approx r$,

$$\begin{aligned} r &\approx \rho_m - \rho_{sm}\hat{\rho}_{sm}\cdot\hat{r} \\ &= \rho_m - \rho_{sm}[\sin\theta_{sm}\sin\theta_m\cos(\phi_{sm}-\phi_m) + \cos\theta_{sm}\cos\theta_m] \end{aligned}$$

Because

$$\begin{aligned} \phi_{sm} &= \phi_s \\ \sin\theta_{sm} &= \frac{\rho_s}{\rho_{sm}}\sin\theta_s \\ \cos\theta_{sm} &= \frac{\rho_s}{\rho_{sm}}\cos\theta_s\frac{\delta Z_m}{\rho_{sm}} \end{aligned}$$

in the phase item of $\frac{e^{-jkr}}{r}$, r can be written as

$$r \approx \rho_m - \rho_s\sin\theta_s\sin\theta_m\cos(\phi_s - \phi_m) - \rho_s\cos\theta_s\cos\theta_m + \delta Z_m\cos\theta_m$$

in the amplitude item,

$$r \approx \rho_m$$

So

$$\frac{e^{-jkr}}{r} \approx \frac{1}{\rho_m}[e^{-jk\rho_m} \cdot e^{jk\rho_s \sin\theta_s \sin\theta_m \cos(\phi_s - \phi_m)} \cdot e^{jk\rho_s \cos\theta_s \cos\theta_m} \cdot e^{\delta Z_m \cos\theta_m}]$$

Appendix C

Calculation of $\hat{\rho}_s \times \hat{\rho}_m$, $\hat{\theta}_s \times \hat{\rho}_m$ and $\hat{\phi}_s \times \hat{\rho}_m$

Refer to Figure 4.2,

$$\begin{aligned}
\hat{\rho}_s &= \sin\theta_s\cos\phi_s\hat{x}_s + \sin\theta_s\sin\phi_s\hat{y}_s + \cos\theta_s\hat{z}_s \\
&= \sin\theta_s\cos\phi_s(\hat{\rho}_m\sin\theta_m\cos\phi_m + \hat{\theta}_m\cos\theta_m\cos\phi_m - \hat{\phi}_m\sin\phi_m) \\
&\quad + \sin\theta_s\sin\phi_s(\hat{\rho}_m\sin\theta_m\sin\phi_m + \hat{\theta}_m\cos\theta_m\sin\phi_m + \hat{\phi}_m\cos\phi_m) \\
&\quad + \cos\theta_s(\hat{\rho}_m\cos\theta_m - \hat{\theta}_m\sin\theta_m) \\
&= \hat{\rho}_m[\sin\theta_s\sin\theta_m\cos(\phi_s - \phi_m) + \cos\theta_s\cos\theta_m] \\
&\quad + \hat{\theta}_m[\sin\theta_s\cos\theta_m\cos(\phi_s - \phi_m) - \cos\theta_s\sin\theta_m] \\
&\quad + \hat{\phi}_m[\sin\theta_s\sin(\phi_s - \phi_m)] \\
\hat{\theta}_s &= \cos\theta_s\cos\phi_s\hat{x}_s + \cos\theta_s\sin\phi_s\hat{y}_s - \sin\theta_s\hat{z}_s \\
&= \hat{\rho}_m[\sin\theta_m\cos\theta_s\cos(\phi_s - \phi_m) - \sin\theta_s\cos\theta_m] \\
&\quad + \hat{\theta}_m[\cos\theta_m\cos\theta_s\cos(\phi_s - \phi_m) + \sin\theta_s\sin\theta_m] \\
&\quad + \hat{\phi}_m[\cos\theta_s\sin(\phi_s - \phi_m)] \\
\hat{\phi}_s &= -\sin\phi_s\hat{x}_s + \cos\phi_s\hat{y}_s
\end{aligned}$$

$$\begin{aligned} = \;& \hat{\rho}_m[-\sin\theta_m \sin(\phi_s - \phi_m)] \\ & +\hat{\theta}_m[-\cos\theta_m \sin(\phi_s - \phi_m)] \\ & +\hat{\phi}_m[\cos(\phi_s - \phi_m)] \end{aligned}$$

Then

$$\begin{aligned} & \hat{\rho}_s \times \hat{\rho}_m \\ = \;& -[\sin\theta_s \sin\theta_m \cos(\phi_s - \phi_m) - \cos\theta_s \sin\theta_m]\hat{\phi}_m \\ & +[\sin\theta_s \sin(\phi_s - \phi_m)]\hat{\theta}_m \end{aligned} \tag{C.1}$$

$$\begin{aligned} & \hat{\theta}_s \times \hat{\rho}_m \\ = \;& -[\cos\theta_s \cos\theta_m \cos(\phi_s - \phi_m) + \sin\theta_s \sin\theta_m]\hat{\phi}_m \\ & +[\cos\theta_s \sin(\phi_s - \phi_m)]\hat{\theta}_m \end{aligned} \tag{C.2}$$

$$\begin{aligned} & \hat{\phi}_s \times \hat{\rho}_m \\ = \;& [\cos\theta_m \sin(\phi_s - \phi_m)]p\hat{h}i_m + \cos(\phi_s - \phi_m)\hat{\theta}_m \end{aligned} \tag{C.3}$$

Appendix D

Integration Formulae

$$\begin{aligned} & \int_0^{2\pi} e^{jk\rho_s \sin\theta_s \sin\theta_m \cos(\phi_s-\phi_m)} \cos(\phi_s-\phi_m) \sin\phi_s d\phi_s \\ = \; & \pi \sin\phi_m [J_0(x_s) - J_2(x_s)] \end{aligned} \tag{D.1}$$

$$\begin{aligned} & \int_0^{2\pi} e^{jk\rho_s \sin\theta_s \sin\theta_m \cos(\phi_s-\phi_m)} \cos(\phi_s-\phi_m) \cos\phi_s d\phi_s \\ = \; & \pi \cos\phi_m [J_0(x_s) - J_2(x_s)] \end{aligned} \tag{D.2}$$

$$\begin{aligned} & \int_0^{2\pi} e^{jk\rho_s \sin\theta_s \sin\theta_m \cos(\phi_s-\phi_m)} \sin(\phi_s-\phi_m) \cos\phi_s d\phi_s \\ = \; & -\pi \sin\phi_m [J_0(x_s) + J_2(x_s)] \end{aligned} \tag{D.3}$$

$$\begin{aligned} & \int_0^{2\pi} e^{jk\rho_s \sin\theta_s \sin\theta_m \cos(\phi_s-\phi_m)} \sin(\phi_s-\phi_m) \sin\phi_s d\phi_s \\ = \; & \pi \cos\phi_m [J_0(x_s) + J_2(x_s)] \end{aligned} \tag{D.4}$$

$$\int_0^{2\pi} e^{jk\rho_s \sin\theta_s \sin\theta_m \cos(\phi_s-\phi_m)} \cos\phi_s d\phi_s = 2j\pi \cos\phi_m J_1(x_s) \tag{D.5}$$

$$\int_0^{2\pi} e^{jk\rho_s \sin\theta_s \sin\theta_m \cos(\phi_s-\phi_m)} \sin\phi_s d\phi_s = 2j\pi \sin\phi_m J_1(x_s) \tag{D.6}$$

$$\int_0^{2\pi} e^{jk\rho_s \sin\theta_s \sin\theta_m \cos(\phi_s-\phi_m)} d\phi_s = 2\pi J_0(x_s) \tag{D.7}$$

where J_n is first kind Bessel function of order n and $x_s = k\rho_s \sin\theta_s \sin\theta_m$.

Appendix E

Power Transmitted by Feed P_T

The feed radiated magnetic field is

$$\begin{aligned}
\vec{H}_f &= (\frac{\epsilon_0}{\mu_0})^{\frac{1}{2}}[E_{\theta_f}(\theta_f,\phi_f)\hat{\phi}_f - E_{\phi_f}(\theta_f,\phi_f)\hat{\theta}_f]\frac{e^{-jk\rho_f}}{\rho_f} \\
&= (\frac{\epsilon_0}{\mu_0})^{\frac{1}{2}}[g_\theta(\theta_s)\cos\phi_f\hat{\phi}_f + g_{\phi_f}(\theta_f)\sin\phi_f\hat{\theta}_f]\frac{e^{-jk\rho_f}}{\rho_f}
\end{aligned}$$

Then

$$\begin{aligned}
P_T &= \int\int \frac{1}{2}Re(\vec{E}_f \times \vec{H}_f)\cdot\rho_f^2\sin^2\theta d\theta d\phi \\
&= \frac{1}{2\eta}\int_0^{2\pi}\int_0^{\pi}(|E_{\theta_f}|^2\cos^2\phi_f + |E_{\phi_f}|^2\sin^2\phi_f)\sin^2\theta_f d\theta_f d\phi_f \\
&= \frac{\pi}{2\eta}\int_0^{\pi}(|E_{\theta_f}|^2 + |E_{\phi_f}|^2)\sin\theta_f d\theta_f \\
&= \frac{\pi}{2\eta}\int_0^{\pi}(|g_\theta|^2 + |g_\phi|^2)\sin\theta d\theta
\end{aligned}$$

where η is the free space impedance.